J. Fluid Mech. (2022), *vol*. 935, A25, doi:10.1017/jfm.2022.13

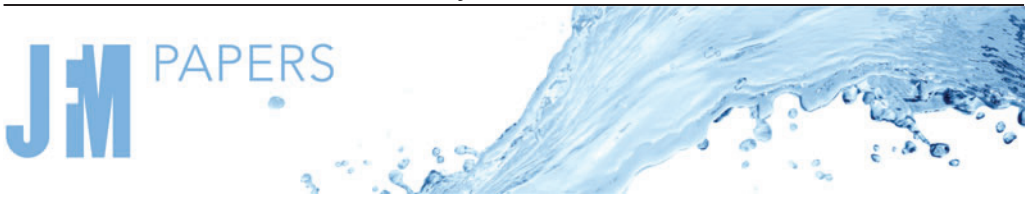

Turbulent spot transit of a hypersonic laminar separation

David Estruch-Samper[1,2,†], Richard Hillier[1] and Leon Vanstone[3]

[1]Department of Aeronautics, Imperial College London, South Kensington SW7 2AZ, UK

[2]Performance and Aerodynamics, Reaction Engines, Abingdon OX14 3DB, UK

[3]Aerospace Engineering Department, University of Texas at Austin, Austin, TX 78705, USA

(Received 23 February 2021; revised 11 December 2021; accepted 22 December 2021)

This paper presents an experimental study of the interaction of turbulent spots with an initially laminar separation, using schlieren visualisation and dynamic measurements of surface heat transfer and pressure. The separation is generated on a blunt cylinder-flare body, tested at Mach 9, and entropy layer effects result in a boundary layer edge Mach number of 3.43 at separation. A single roughness element is used to produce isolated spots, defined such that separation collapse and re-establishment is completed before arrival of the next spot. On average the spot axial length, at the start of the interaction, is 2.5 times the separation length, growing to 6.8 times as the spot base passes the original reattachment position. As such the spot comprises a large perturbation. The local separation responds almost immediately with passage of the spot, so that the downstream region may be unaffected while the upstream part has already collapsed. Re-establishment of separation is slow, taking up to four times the total transit time of the spot. A basic model is presented to explore the transient wave processes during spot passage.

Key words: high-speed flow, compressible boundary layers, hypersonic flow

1. Introduction

Laminar-turbulent transition has a critical effect on the aerothermodynamics of hypersonic flight and as such is the subject of extensive research, both experimental and computational. Classic test cases include the flat plate (e.g. Franko & Lele 2013; Chuvakhov, Fedorov & Obraz 2018) and the sharp cone (e.g. with half-angles of 5°–7° in Sivasubramanian & Fasel 2015; Hader & Fasel 2019). The Hypersonic International Flight Research Experimentation (HIFiRE)-5b has documented transition on a sharp-nose vehicle (Kimmel *et al.* 2018) from heat flux measurements, including turbulent overshoots and defining a connection between transition length and turbulent spot generation rates

† Email address for correspondence: david.estruch-samper@reactionengines.co.uk

(Juliano, Jewell & Kimmel 2021). Other geometries, including concave surfaces and swept leading edges, are broadly relevant to hypersonic vehicle design (e.g. the Skylon concept spaceplane, ESA 2011) and are as well notably being considered under the Boundary Layer Transition (BOLT) flight experiment (Wheaton *et al.* 2021). The mechanisms of transition in blunt bodies, such as blunt cones or re-entry capsules, present a number of distinct characteristics that render them difficult to predict (Leidy *et al.* 2017; Paredes, Choudhari & Li 2020*a*). Regions involving flow separation are commonplace, but the physics of separated transitional boundary layers remains less well understood. The objective of this work is to establish a two-dimensional (axisymmetric) laminar separation, over a blunt body of revolution at Mach 9, which is then perturbed by incoming turbulent spots.

Transition to turbulence can occur through different mechanisms, ranging from modal growth of relatively weak boundary layer instabilities – such as Görtler vortices, cross-flow instabilities, first and second Mack modes (Mack 1984) – to strong disturbances that bypass the more moderate processes and abruptly trip the flow to a turbulent state (Reshotko 2001). Short roughness elements can introduce transient perturbations that are nonlinear in nature and that may grow to prompt transition (Tumin 2007), while taller 'effective' elements force transition at a finite distance close downstream within their wake, in which case absolute instability is likely to dominate (Wheaton *et al.* 2011). Theoretical models of transient growth for roughness-induced transition generally rely on analysis of optimal perturbations, associated with the streamwise vortices in the element's wake, aided by empirical correlations (Tumin 2008). Further efforts to model the receptivity of the boundary layer, in terms of kinetic fluctuations in the associated stress tensors and heat fluxes, have gone to characterise the generated small-scale flow perturbations and their amplification via nonlinear effects towards transition (Fedorov & Tumin 2017). Detailed insight on the various transition pathways of high-speed flows may be found in the reviews by Schneider (2008) and Fedorov (2011), and more recently by Lee & Jiang (2019).

The present investigation falls within an intermediary stage in which laminar disturbances with significant amplitude experience transient growth and bypass the earlier mentioned mechanisms to break down into patches, or spots, of turbulent flow. Turbulent spots are key elements in the classical transition process and were identified originally in incompressible flow studies by Emmons (1951). They generally exhibit a characteristic arrowhead planform that is understood to be a result of a 'cascading' effect whereby upstream disturbances foster the development of new disturbances as the spot convects in the streamwise direction (Perry, Lim & Teh 1981). Turbulent spot growth is thus inherently influenced by classical entrainment as well as by destabilisation of the surrounding laminar flow, with lateral spreading rates substantially greater than the wall-normal growth (Gad-El-Hak, Blackwelder & Riley 1981). Retardation of the near-wall flow induces a growing streamwise elongation of the spot, leading to coalescence with neighbouring spots and the eventual formation of fully turbulent flow (Narasimha 1985).

As depicted in figure 1, the internal organisation of well-developed spots exhibits a front overhang region, followed by a turbulent core with lateral wing tips and a calmed wake at its rear. The overhang and wing tip organisation is driven by near-wall flow retardation, and the calmed region behind the arrowhead structure is more elongated near the centreline. Fischer (1972) showed that the lateral growth rate of turbulent jets/wedges decreased with increasing supersonic Mach number, and such low spreading rates have been observed consistently for turbulent spots in hypersonic experiments, including Mee (2002), Casper, Beresh & Schneider (2014) and Jewell, Leyva & Shepherd (2017) as well as those preceding the present investigation (Fiala *et al.* 2006; Fiala, Hillier & Estruch-Samper 2014). Direct numerical simulations (DNS) by Krishnan & Sandham (2006, 2007) and

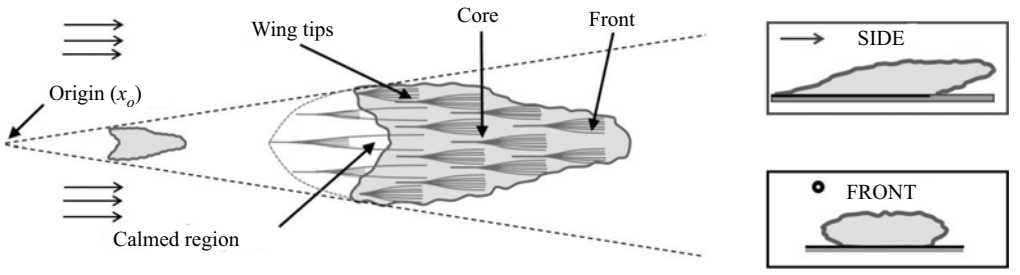

Figure 1. Schematic of turbulent spot substructures based on the conceptual model by Perry *et al.* (1981). Spot with origin at the inception location x_o.

Redford, Sandham & Roberts (2012) have shed light on the mechanisms for formation of new disturbances and on the spot substructures. Krishnan & Sandham (2007) also used computational fluid dynamics (CFD) to study the effect of turbulent spots on a shock-wave-induced separation and found that the associated adverse pressure gradient has a generally destabilising influence on the spot, in agreement with earlier observations from incompressible flows (Seifert & Wygnansky 1995). This was corroborated in the hypersonic tests by Butler & Laurence (2020) on a 5° half-angle cone, where it was observed that corner flow separation over a 15° half-angle flare promoted rapid breakdown of instability waves upon reattachment, while expansion regions had a stabilising effect on the disturbances.

DNS has proven a particularly useful tool to provide insights of hypersonic transition where ground testing may be challenged to obtain non-intrusive information at high spatial resolution. In Franko & Lele (2013), the development of streamwise streaks and their breakdown to fully turbulent flow was investigated for a Mach 6 flat plate boundary layer, noting a heat transfer overshoot similar to the tendencies observed in past experiments; and likewise Sivasubramanian & Fasel (2015) established that the fundamental breakdown to turbulence is a viable mechanism in sharp cone configurations at the same Mach number. Novikov, Egorov & Fedorov (2016) conducted DNS of three-dimensional (3-D) wave packets over a Mach 5.4 compression corner, and found that nonlinear effects could destabilise the wave packet in the separation region and lead to its breakdown downstream of reattachment, prompting the formation of a young turbulent spot in the reattached flow region when sufficiently strong forcing was applied; the authors concluded that the wave packet contents and its downstream evolution depend strongly on how and where the initial disturbance is excited. Along these lines, Chuvakhov *et al.* (2018) assessed the suitability of different unsteady boundary conditions for DNS modelling of the nonlinear breakdown of unstable wave packets into turbulent spots over a Mach 6 flat plate boundary layer. And Hader & Fasel (2019) further resolved the formation of streamwise high skin-friction and heat-transfer streaks over a flared cone at the same Mach number, arguing that the fundamental breakdown to turbulence is likely to be a dominant path to transition under low-noise (‘quiet’) conditions.

Recent ground test studies have, on the other hand, looked into the fluid–structure interaction associated with the passage of turbulent spots. In the experiments by Casper *et al.* (2018) on a 7° half-angle cone at Mach 5–8, the surface response to the passage of spark-generated spots was characterised by accelerometers on the backside of a panel. Under ‘quiet’ Mach 6 conditions, the flow remained laminar and spots excited a directionally-dependent panel response, but this was masked by acoustic perturbations in other higher-noise facilities, where a clear structural response was seen only for spot

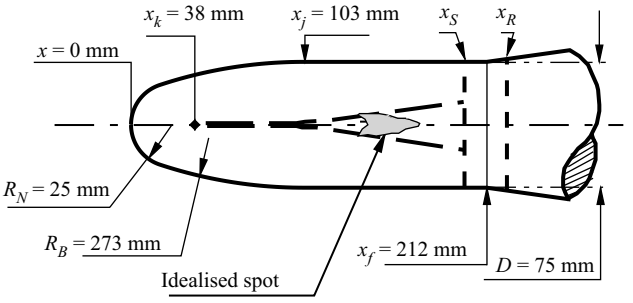

Figure 2. Test geometry. Body of revolution with spherically blunted nose, radius $R_N = 25$ mm, blended by an arc, radius $R_B = 273$ mm, to a cylindrical section of diameter $D = 75$ mm. The blending-arc/cylinder junction (x_j) is at 103 mm. Design iteration selected an 8° angle flare (α_f) with cylinder–flare junction (x_f) at 212 mm. The axial separation and reattachment positions, x_S and x_R, are estimated as 200.5 mm and 223.5 mm, respectively. The roughness element location (x_k) is 38 mm. Long-dashed lines show an idealisation for the trajectory of spot formation, with an effective origin close to x_j.

passage rates near the natural frequency of the panel. Subsequent studies on a slender cone found good agreement between numerical estimates of the cone structural response and experimental damping times and acceleration amplitudes (Robbins, Casper & Mesh 2019), again concluding that higher rates of spot generation lead to enhanced response near the structure's natural modes. Similar observations were noted by Whalen *et al.* (2020) in their experimental tests on a flexible panel exposed to a Mach 6 ramp-induced shock-wave/boundary-layer interaction.

Within the context of transition in hypersonic blunt bodies, significant progress in the understanding of discrete roughness effects and relevant correlations was made during the Shuttle programme (Berry & Horvath 2008; Horvath *et al.* 2012). More recently, Leidy *et al.* (2017) considered the transition over a blunt body modelled after the Orion capsule at re-entry conditions and related the local flow properties and roughness heights to established transient growth scalings; while Radespiel *et al.* (2018) assessed the effects of roughness over spherical Apollo-type capsule models for a range of experimental studies at different hypersonic facilities, finding good evaluation against transient growth theory and numerical simulation data. DNS of transition over similar re-entry capsules has provided insights into the generation of stationary roughness-induced disturbances and the evolution of unsteady perturbations (Hein *et al.* 2019). Yet, as noted by Paredes *et al.* (2020*a*), the planar Mack-mode instabilities that more commonly dominate transition in sharp cone geometries can suffer a reduction in modal growth in blunt configurations, yielding a more complex environment where both planar and oblique convecting disturbances may experience substantial amplification. The presence of separation regions as in the present case inevitably adds to the complexity of the problem.

2. Computational and experimental details

2.1. *Computational method*

The geometric details of the test model are provided in figure 2. Everywhere the attached (pre-separation) boundary layer is less than 2 mm thick, making experimental profile or thickness measurements non-viable. Similarly, there were no means available to measure separation and reattachment positions accurately. These are all critical defining elements for separated flow studies, however, so that laminar CFD has been employed to provide support to the experimental work. It also provided a central role in the initial model design decisions.

A second-order (space and time) finite-volume code was used, assuming axial symmetry, with a mesh of quadrilateral cells in the (x, r)-plane. A generalised Riemann problem (Ben-Artzi & Falcovitz 1984; Hillier 2007) provided inviscid fluxes at cell interfaces with centred differencing used for the diffusive terms. It is time-marched to steady state from an impulsive start at free stream conditions. An adaptive mesh strategy was used to refine resolution in important areas. The finest mesh (A) used 1000 cells along the body surface from the stagnation point to a chord distance of 250 mm, with 140 cells covering the predicted 23 mm distance from separation (x_S in figure 2) to reattachment (x_R). It also provided, over the full chord length, both 500 cells from the body surface to the bow shock wave and also a minimum of 110 cells from the body surface to the outer edge of the viscous layer. At the cylinder–flare junction position, virtually at mid separation length, converged results showed that there were 48 cells from the surface out to the maximum reverse flow position, a further 30 cells to reach the separation streamline, and a further 45 cells to reach the edge of the free shear layer. Clearly, confirmation of mesh convergence is important, and mesh B was generated by combining local clusters of four cells, from mesh A, into one cell, with mesh C resulting from a similar coarsening of mesh B. Heat transfer is a sensitive measure of mesh convergence, and the CFD results, in figure 3(b), show that predictions for meshes A and B are virtually indistinguishable; only downstream of reattachment ($x \approx 230$ mm) is a difference visible of approximately 1.5 %. Mesh C, the coarsest option, shows a visible, but still slight, difference. For pressure (figure 3a), the meshes A and B effectively overlay each other over the full chord range with practically no difference evident for mesh C. Thus mesh A is assumed to correspond very closely to the mesh-converged steady, laminar axisymmetric solution and provide the results presented.

2.2. *Gun tunnel facility*

The Imperial College gun tunnel uses Nitrogen test gas. Flow total pressure and temperature ($P_{0,\infty}$, $T_{0,\infty}$) are monitored, and reproduced closely, from run to run, and are given in table 1. Flow characterisation is completed by Mach number definition, usually achieved through Pitot probe or static pressure probe measurements. Both can cause issues, and here the no-flare model was employed in a secondary role as a calibration probe. CFD (as described in § 2.1), using simulations at free stream Mach numbers, M_∞, 8.9, 9.0 and 9.1, determined that a value of 9.025 gave the best fit to the measured no-flare surface pressure data. In such an approach it is essential that full Navier–Stokes simulations are employed since the boundary layer induced contribution to the pressure can be significant. This calibration ensured, of course, that surface pressures upstream of separation would match closely between CFD and experiment. This process used no further data measured on the model, be it surface heat transfer or data produced with the flare configuration. Detailed spatial calibration by Mallinson *et al.* (2000) also showed a weak axial Mach number gradient that is barely significant for the present short chord model, causing only an approximate 4 % fall in static pressure along the model up to the end of the instrumented section at $x = 250$ mm. Total run duration is 25 ms, with an established flow window of approximately 6 ms. The Prandtl number Pr is assumed constant at 0.72, and the viscosity is evaluated using Keyes (1952). The full tunnel conditions used in data reduction and CFD are summarised in table 1.

2.3. *Model and instrumentation*

The basic no-flare model, that is, the blunt-nose-cylinder element of figure 2, already existed from earlier transition studies (Fiala *et al.* 2006, 2014). The 25 mm nose radius

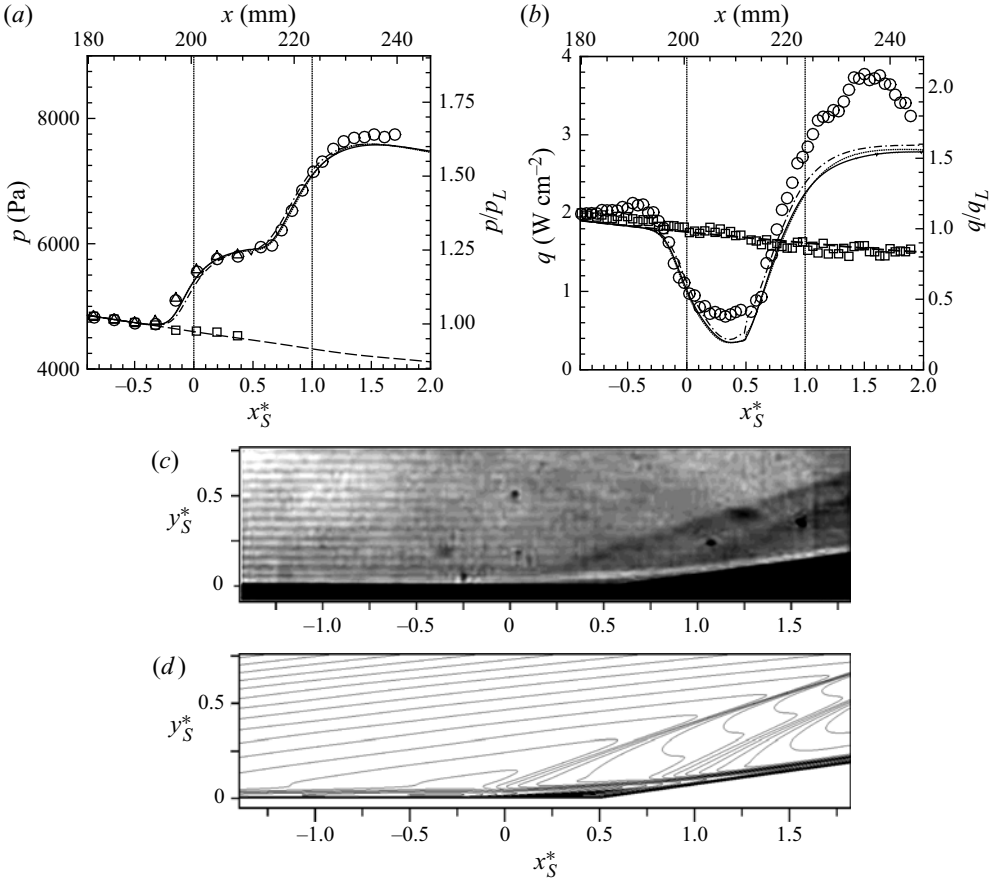

Figure 3. Reference laminar data (no roughness element). (*a*,*b*) Flare case: axial distributions for mean surface pressure and heat transfer, experiment (◯) and CFD (dashed-dot, dashed and solid lines for progressive mesh refinement from mesh *C* through mesh *B* to mesh *A*). Experimental surface pressure on the opposite side of the model to assess alignment (Δ). No-flare case experiment (□) and CFD with mesh *A* (long-dashed line). (*c*) Schlieren of separation zone. (*d*) Density contours from CFD.

M_∞	$\mathrm{d}M_\infty/\mathrm{d}x$ (m^{-1})	$P_{0,\infty}$ (MPa)	$T_{0,\infty}$ (K)	T_w (K)	Re_∞ (m^{-1})
9.025 ± 0.025	0.24 ± 0.03	60.8 ± 1.2	1150 ± 45	293 ± 5	$46.0 \times 10^6 \pm 6\,\%$

Table 1. Nominal flow conditions: free stream Mach number M_∞, axial Mach number gradient $\mathrm{d}M_\infty/\mathrm{d}x$, total free stream pressure $P_{0,\infty}$, total free stream temperature $T_{0,\infty}$, wall temperature T_w, and unit free stream Reynolds number Re_∞.

R_N was chosen to be very large compared with the boundary layer thickness and almost completely avoids entropy layer 'swallowing' over the measurement length. The nose is blended to the cylindrical afterbody, diameter $D = 75$ mm, by a constant radius arc R_B of 273 mm that maintains continuity of body slope at matching points $x = 17.2$ mm and $x = 103$ mm, and provides a monotonic fall of pressure from the nose stagnation point ($104p_\infty$) to the test region over the cylinder body ($p \approx 1.6p_\infty$), where p_∞ is the free stream static pressure.

x (mm)	M_e	Re_e (m^{-1})	U_e/U_∞	T_e/T_w	δ_x (mm)	$\delta_{1,x}$ (mm)	$\delta_{2,x}$ (mm)	$q_{L,x}$ (W cm^{-2})	Re_{δ_2}/M_e
$x_k = 38$	2.30	6.6×10^6	0.73	1.87	0.40	0.08	0.05	11.2	156
$x_j = 103$	3.17	3.8×10^6	0.83	1.40	1.13	0.29	0.12	2.99	144
$x_f = 212$	3.43	3.3×10^6	0.85	1.14	1.88	0.61	0.20	1.72	185

Table 2. Laminar CFD-evaluated reference properties for the no-flare model at roughness element location x_k, nose–cylinder junction x_j, and cylinder–flare junction x_f. Properties include: edge Mach number M_e, unit Reynolds number with properties evaluated at boundary layer edge Re_e, edge to free stream velocity ratio U_e/U_∞, edge to wall temperature ratio T_e/T_w, local boundary layer thickness δ_x (at given 'x' station), displacement and momentum thicknesses $\delta_{1,x}$ and $\delta_{2,x}$, laminar heat transfer $q_{L,x}$, and ratio of momentum thickness Reynolds number to edge Mach number Re_{δ_2}/M_e.

Table 2 lists reference properties at three salient x locations, for the no-flare case. These are: x_k (38 mm), the final location selected for the use of the roughness element; x_j (103 mm), the blending arc–cylinder junction; and x_f (212 mm), the final selected position for the cylinder–flare junction. The table includes boundary layer thickness estimates extracted from the CFD. Since the flow is rotational between the boundary layer edge and the bow shock, edge conditions are taken at the predicted position of 99.5 % recovery of total enthalpy h_0 from the wall, that is, $(h_0 - h_w) = 0.995(h_{0,\infty} - h_w)$. Boundary layer thickness δ_x, edge velocity U_e and other edge properties are determined based on this definition.

The cylinder–flare design addressed three constraints.

(1) Turbulent spots had to be well developed by the time they reached the measurement region and large enough to ensure satisfactory spatial resolution. As such, a minimum position for the cylinder–flare junction was enforced with $x_f \geq 200$ mm. By this stage, for the given roughness element conditions described in § 4.1, the spot width and length were expected to be respectively of orders 20–25 mm and 40–75 mm.
(2) The flare angle α_f, and hence the separation scale, should be large enough for good resolution of the interaction. A minimum of 6° was enforced to ensure sufficient margin above the incipient separation angle.
(3) The separation scale should be small enough to ensure full re-establishment, after spot-induced collapse, within the 6 ms tunnel test window.

Constraints (2) and (3) are in conflict, but (3) is the most critical, and a maximum establishment time of 2 ms was enforced. The design issues were addressed by a mix of schlieren visualisation of prototype models and time-accurate laminar CFD (§ 2.1) assuming an impulsive flow start. The final selection chose a 'safe' option of an 8° flare located at $x_f = 212$ mm, giving a predicted separation length, L_S, of 23 mm. From the CFD the separation length establishes within 1% of its asymptotic value in 2 ms; experimentally, re-establishment was faster, probably because the simulation was axisymmetric while the actual process is three-dimensional.

Surface heat transfer measurements used platinum thin-film gauges on a *Macor* substrate as: (a) an axial array of up to 64 gauges pitched at 1 mm spacing and with sensor element size $\Delta x = 0.1$ mm by $\Delta z = 2$ mm; and (b) an 18-gauge circumferential array spaced at 4 mm (6.1°) in azimuth and with spatial resolution $\Delta z = 2.5$ mm. These sensors registered 90 % of a step change in surface heat transfer in 11 μs (Schultz &

Jones 1973), and the measured surface temperature history was reduced digitally to heat transfer (Cook & Felderman 1966; Schultz & Jones 1973) with an estimated error of ±10%. Pressure measurements used Kulite XCS-062 miniature transducers located just below the surface, with a tapping diameter of 0.5 mm, as: (a) an axial array at a pitch of 2 mm; and (b) one axial array of sensors with a pitch of 4 mm, over the cylindrical section on the opposite side of the model, to aid alignment. The expected error in the pressure measurements is ±3.5% with an estimated frequency response of 80 kHz for the tapping/dead-volume/transducer combination. Sensor outputs were amplified and low-pass filtered at 50 kHz before digitising through a 24-bit analogue-to-digital converter at a sample rate of 100 kHz.

3. Reference laminar separation

3.1. *Model surface conditions and alignment with free stream*

Considerable effort was made to ensure laminar conditions. The model was highly polished, its surface finish ensuring an average roughness <0.5 μm, and the test section kept clean and free of contaminating particles between runs. Initially, it was found that turbulent spots could be triggered by disturbances produced by particles released at the initial rupture of the *Melinex* (polyester film) nozzle-throat diaphragms, so these were replaced by stainless steel diaphragms with a better rupture behaviour.

The model was aligned geometrically with the nozzle axis within ±0.05° in pitch and yaw and within 0.5 mm in translation. Figure 3(*a*) presents various data but the specific ones related to model alignment are the axial distribution of surface pressure from the main row of tappings (on the top of the model) together with the more restricted axial row at 180° in azimuth (on the bottom). These cover both attached and separated flow segments. They show almost exact agreement between the two sets of tappings, and confirm excellent alignment of the model in pitch. It also supports the decision to use a body of revolution to produce the best possible two-dimensional (i.e. axisymmetric) flow. There were no tapping rows on each side of the model so aerodynamic alignment in yaw cannot be confirmed categorically although geometric alignment is as precise as in pitch.

3.2. *Surface pressure and data normalisation*

Axial distributions of average pressure and heat transfer are presented in figures 3(*a*,*b*) for tests on the blunt cylinder flare and the basic blunt cylinder body without the flare. From here on, they are referred to simply as the *flare* and *no-flare* cases. Because of the calibration process, experiment and CFD for pressure for the no-flare case (figure 3*a*) are essentially in precise agreement. For the flare case, the CFD predictions for pressure again agree closely with the measurements (figure 3*a*). It therefore seems most unlikely that the CFD-predicted positions for separation and reattachment should differ significantly from the actual experimental values. Therefore, in the absence of direct measurement of separation and reattachment positions and separation length (x_S, x_R, L_S), all references to these refer to CFD-predicted values. These are given in table 3. It is difficult to place an accuracy estimate on this procedure. However, the small discrepancy between CFD and experiment places the initial measured separation pressure rise ($195 \leq x$ (mm) ≤ 205) slightly upstream of the CFD prediction, while the measured reattachment rise is shifted ($215 \leq x$ (mm) ≤ 225), by an even smaller amount, slightly downstream. This would amount potentially to an underestimate of experimental separation length by CFD of approximately 5 % or 1.2 mm.

x_S (mm)	x_R (mm)	L_S (mm)	H_S (mm)	$\delta_{1,L}$ (mm)	q_L (W cm^{-2})	p_L (Pa)
200.5	223.5	23	0.78	0.61	1.80	4720

Table 3. Reference data for $\alpha_f = 8^\circ$ flare with cylinder–flare junction at $x_f = 212$ mm. The base laminar heat transfer and pressure q_L and p_L correspond to the undisturbed (attached) flow values taken from experiment at x_S on the blunt cylinder without the flare. The remainder of values given are from CFD; H_S is the normal distance from the cylinder–flare junction to the separation streamline, and $\delta_{1,L}$ is the displacement boundary layer thickness at x_S (i.e. $x_S^* = 0$). Here, x_S and x_R are based on the zero skin-friction coefficient $C_f = 0$ criterion.

In figure 3, and following, the axial distance (x) is presented both in dimensioned form and also normalised by the CFD predicted separation/reattachment scales, so that x_S^* values 0 and 1 correspond respectively to separation and reattachment. Similarly, z_S^* and y_S^* denote the transverse circumferential distance from the centreline, and the body normal distance, both normalised by L_S. Surface pressure (p) and heat transfer (q) are likewise presented in dimensioned form and also normalised by the reference values (p_L and q_L), taken on the no-flare model but at the separation position identified for the flare case. These reference values are also listed in table 3. As a final observation on the pressure distribution, the lack of a clear plateau in the pressure distribution (between the separation and reattachment pressure rises) is characteristic of the separation length, L_S, being modest in scale compared to the boundary layer thickness, $L_S/\delta_0 = 12.2$.

3.3. *Surface heat transfer*

Figure 3(b) shows a very close match between CFD and experiment for heat transfer for the no-flare case. For the flare case, however, CFD underpredicts heat transfer in three segments.

(1) There is a small (in amplitude and streamwise scale) effect centred at $x_S^* \approx -0.4$, which is the position where the separation pressure rise begins (figure 3a).
(2) In the separation zone, both CFD and experiment show a minimum at the same position ($x_S^* \approx 0.35$), but CFD clearly underpredicts experiment.
(3) Approaching reattachment, measured heat transfer rises well above CFD to reach a maximum at $x_S^* \approx 1.5$, then falls rapidly with every likelihood of meeting the CFD distribution shortly beyond the end of the instrumented section.

Two critical assumptions in the CFD modelling are that the flow is both axisymmetric and laminar. Departure from axisymmetry due to incidence or yaw has been excluded previously. A 3-D effect (i.e. non-axisymmetry), which has appeared in separated flows over a broad range of Mach numbers, is streamwise cellular structures or Goertler-type vortices. Figure 4 presents a typical surface oil flow taken during a run. Clearly, there are issues with using oil flows in a short duration facility, and resolution was insufficient to produce features that could be identified as separation/reattachment, but it does indicate a series of streamwise structures with spanwise spacing about twice the pre-separation boundary layer thickness. Such structures have been identified in a range of separation studies, both laminar and turbulent, including the rearward-facing step (Roshko & Thomke 1966), several studies in the present facility (Denman 1996; Jackson, Hillier & Soltani 2001; Murray, Hillier & Williams 2013), a range of interactions reviewed in Babinsky & Harvey (2014), and in analysis by Dwivedi *et al.* (2019) on a

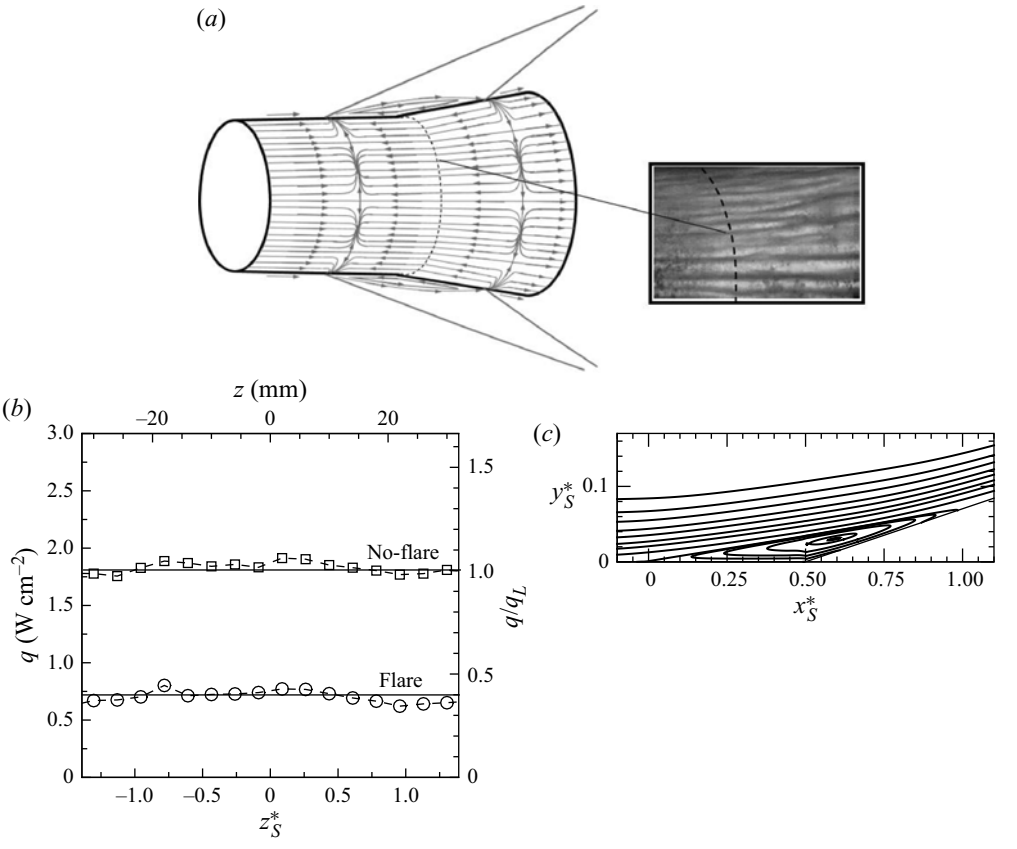

Figure 4. (*a*) Schematic of near-wall flow structures together with oil flow visualisation. (*b*) Transverse profiles of mean heat transfer at $x_S^* = 0.2$ for flare, ◯, and no-flare, □. (*c*) CFD streamlines, the topmost originating at the boundary layer edge at $x_S^* = -0.5$ (note also the 2 : 1 stretching between the two axes).

laminar hypersonic compression-ramp separation. Spanwise distributions of heat transfer, shown in figure 4(*c*), show no indication of periodic structures, with no difference in uniformity between flare and no-flare cases. This could reflect several causes, amongst which could be gauge resolution issues or that the effect of structures is weak and the fact that streamwise structures may not be fixed, but instead could drift back and forth around the circumference, whereas in the oil flow the establishment of the surface oil flow pattern may well fix the location of the structures themselves.

Having identified that streamwise structures are almost certainly a basic characteristic of the flow, the issue remains as to whether transition is also a contributor to the CFD–experiment discrepancy. The close agreement between experiment/CFD pressure in figure 3(*a*) suggests that any effect is weak. In addition, the measured fall in heat transfer as separation is passed is characteristic of laminar separation and, at least initially, is well duplicated by CFD. The most problematic area is the clear overshoot in heat transfer as reattachment is passed. This could be either the effect of reattachment on streamwise structures or the onset of transition provoked by reattachment. It does, however, reach a heat transfer maximum at $x_S^* \approx 1.5$, after which the trend is such that it appears to be returning to the laminar CFD prediction. Possibly it is a warning of more severe effects for further increases in flare angle so that the 'safe' choice of an 8° flare seems justified.

3.4. *Basic length scales defining separation*

In addition to the separation length, L_S, there are two further length scales that complete the large-scale description of the separation region. The spanwise scale of separation, S_S, reflects the importance of 3-D effects. In the present case, S_S is the circumferential distance around the model. This is large compared with the separation length, $S_S \approx 10.25L_S$. During the interaction with an isolated spot it will be seen that the total transverse width of collapsed separation is $\approx 1.4L_S$ so that the bulk of the circumference remains separated. In addition, although during the interaction pressure signals could potentially propagate directly around the circumference in the 'wave tube' comprised by the separation, this gives a total circumferential propagation time that is approximately 4.8 times the complete transit time of a mean spot through separation and also slightly larger than the separation collapse/recovery time found later. Thus any effects of the model span/circumference are expected to be negligible. During transient experiments no disturbance was detected at 180° in azimuth from the test segment. The third defining length scale for a separation is a measure of the distance from the surface to the separation streamline. We define this here as H_S, the normal distance from the cylinder–flare junction to the separation streamline. This is taken from CFD and gives $L_S/H_S = 29.5$ (also given in table 3), showing the very shallow nature of the separation bubble. This is also evident in the computed streamlines of figure 4(*c*) and in both the schlieren and computed wave field in figures 3(*c*,*d*).

4. No-flare case: definition of turbulent spot characteristics

4.1. *Design for single roughness element*

In Fiala *et al.* (2014), a square planform (2 mm side length) 'diamond-orientation' roughness element was located at $x_k = 38$ mm on the no-flare model. This is indicated in figure 2. This is a location sufficiently far from the nose that the boundary layer edge Mach number is now supersonic ($M_e \approx 2.28$) and in a region of strong favourable pressure gradient $\beta = -0.38$, where

$$\beta = \frac{\delta_1}{\tau_w}\frac{\mathrm{d}p}{\mathrm{d}s}, \tag{4.1}$$

as given in Laderman (1980). Here all quantities are evaluated from CFD, with s the wetted distance along the surface and τ_w the surface skin friction.

Varying the element height k provided the following:

(a) for $k = 40$ μm, the flow remains laminar;
(b) for $k = 60$ μm, an intermittent wedge forms, comprising clear trains of turbulent spots with effective origin close to the start of the cylindrical section x_j;
(c) for 80 μm $\leq k \leq$ 120 μm, a turbulent wedge forms, with an outer spreading half-angle $\alpha_o \sim 7°$ and an effective origin again near x_j; and
(d) for $k = 240$ μm, the turbulent wedge maintains a similar spreading angle but now, through bypass transition, with its effective origin close to the roughness element.

From the $Re_{\delta_2}/M_e \times k/\delta_k = 70 \pm 20\,\%$ correlations in Berry & Horvath (2008), the shortest element height at x_k to induce bypass transition is $k \approx 180$ μm, consistent with (c) and (d). The reference to outer spreading angle in (c) relates to the fact that the spot comprises a fully turbulent core with an outer intermittent region where the flow conditions switch between those characteristic of the surrounding laminar flow and those characteristic of the central core.

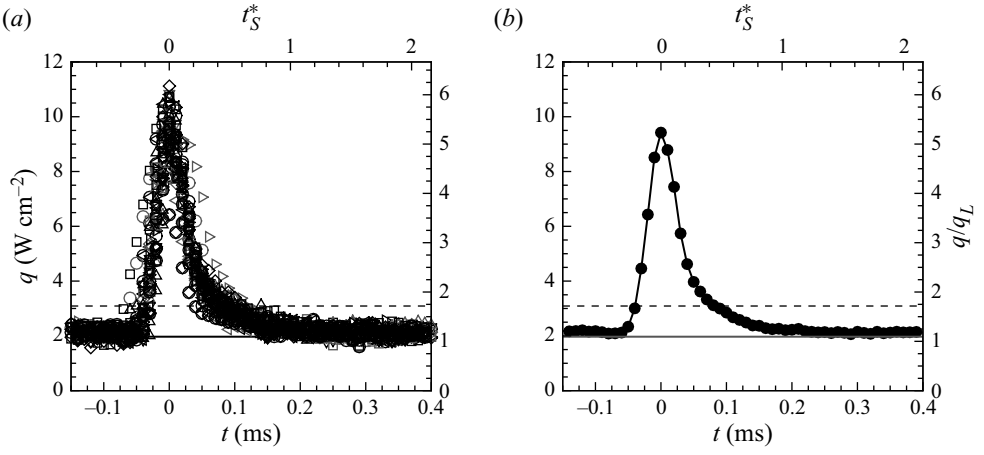

Figure 5. No-flare case. (*a*) All isolated spot heat transfer histories at $x_S^* = -0.5$. (*b*) Data-averaged version of (*a*). The solid line is the fully laminar (no roughness element) value at this position, and the dashed line is the 1.6 factor threshold for spot detection. Time $t = 0$ is set at the instant that the peak heat transfer position reaches the sample location.

For the present study, the element position of $x_k = 38$ mm was retained. Element height (c) above was used to acquire a limited comparative data set for the fully turbulent wedge. For the isolated spot, a delicate iteration was required to identify the best element height. The issue here is that the isolated spot requires that in the interval between preceding and following events, the flow returns to its reference laminar state. Given the approximately 2 : 1 speed ratio between spots front and back, even cases with relatively low spot inception rates will eventually coalesce downstream to form an embryonic, and then full, turbulent wedge. It required careful adjustment of element height to delay this beyond the measurement region. The roughness element height eventually used was 46 μm ($k/\delta_k = 0.115$), in the regime between (a) and (b) above. This gives a roughness-height Reynolds number $Re_{kk} \approx 300$ (evaluated with properties at roughness height). This is of the order of the critical Reynolds numbers seen in recent studies on hypersonic blunt-body transition (Paredes *et al.* 2020*b*).

4.2. *No-flare case: definition of incident spot characteristics along centreline*

Using the element height determined in § 4.1, figure 5(*a*) shows the ensemble of isolated spot heat transfer histories, for the no-flare case, at $x_S^* = -0.5$ ($z_S^* = 0$). Zero-time is taken at the instant of maximum heat transfer q_{max}. The corresponding average isolated spot is presented in figure 5(*b*). A rapid heat transfer increase is produced at the initial arrival of the spot front, with a slower final recovery in the base/wake. Both pre- and post-spot data clearly asymptote to the (no-roughness element) reference laminar level satisfying the isolated spot requirement. Data scatter in figure 5(*a*) reflects measurement errors, in part connected with the high-speed passage of the spot, as well as variations in spot scale. Given that the frequency of spot passage at the sensor array is several orders of magnitude lower than the anticipated instability frequencies at the roughness element position, x_k, it is plausible that packets of high-frequency disturbances form, likely driven by local shear and cross-flow within the element's wake (Estruch-Samper *et al.* 2017). Each packet then evolves into a spot, and measured spot variations at the sensors are partly a measure of the length and intensity of these initial packets.

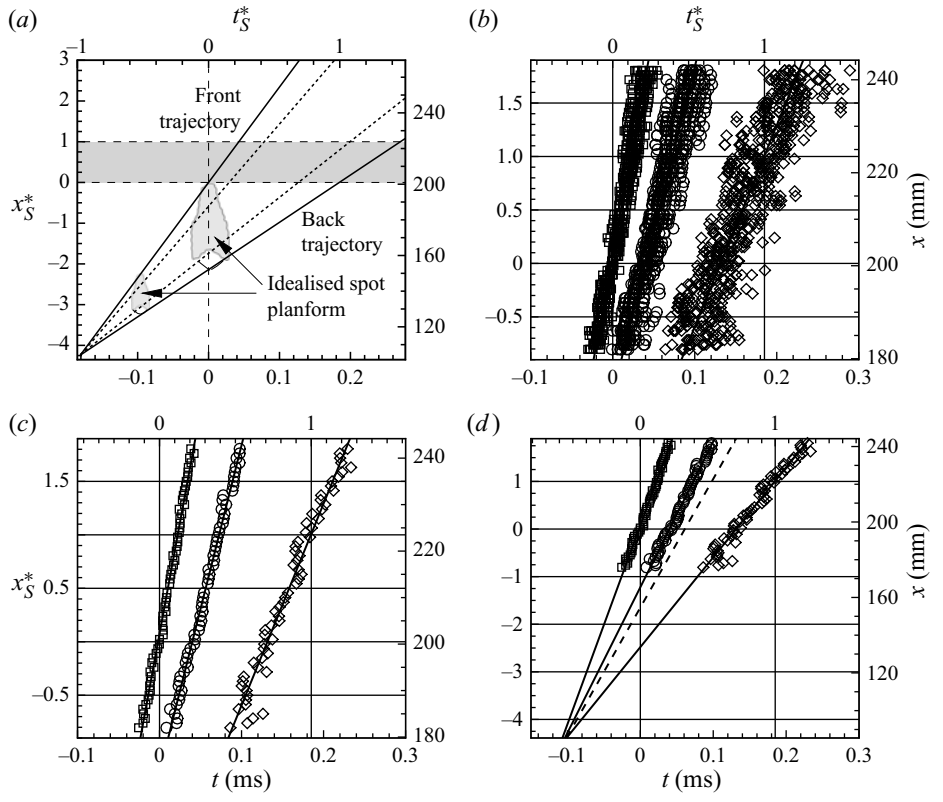

Figure 6. No-flare case. Data for propagation of isolated spots using the full axial array of sensors. (*a*) Idealised schematic of growth of spot fronts and backs over the zone of interest, with solid and dashed lines showing outer (intermittent) and inner (fully turbulent) interfaces. (*b–d*) Measured x–t trajectories for fronts □, backs ◊, and axial location of peak heat transfer ○. Time $t = 0$ established when spot front reaches $x_S^* = 0$. (*b*) Ensemble of all data. (*c*,*d*) Linear fit to averaged data. In (*d*), dashed line indicates estimated trajectory of maximum width position.

Figure 6(*a*) presents idealised front and back trajectories in the (x, t)-plane, using the full axial row of heat transfer gauges, with their trajectory slope giving the appropriate front/back velocities. There is no simple surface heat transfer criterion to define a non-spot/spot interface and, furthermore, above the surface spots feature front/side 'overhangs' that extend beyond the surface thermal footprint. For consistency with original work on the blunt cylinder model in Fiala *et al.* (2006), a spot threshold of 1.6 times the local laminar value is used, high enough to avoid spurious detection through sampling noise and turbulent fluctuations. Given that the highest surface heat transfer levels for a spot are of order five times the laminar level, a threshold factor of 1.6 probably places the measurement in the outboard part of the intermittent zone. Figures 6(*b–d*) present the measured trajectories for fronts and backs using the full axial sensor array, with zero time $t = 0$ defined as the instant that the front of each individual spot reaches $(x_S^* = 0)$. These give a virtual inception position of $x_S^* \approx -4.5$, near the start of the cylindrical section at x_j as in figure 2.

When the spot front reaches $x_S^* = 0$, the average spot length is $\approx 2.5 L_S$, increasing to $\approx 3.0 L_S$ when the spot front reaches $x_S^* = 1.0$. Extrapolating the data beyond the last measurement station ($x \geq 240$ mm), this increases to $\approx 5.6 L_S$ when the spot back reaches

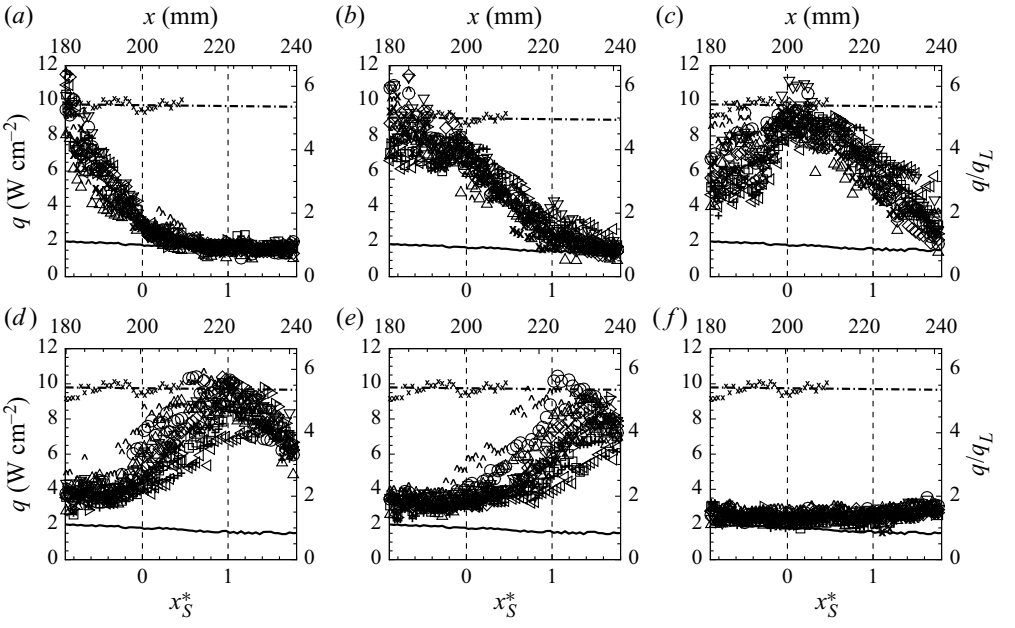

Figure 7. No-flare case, isolated spots. Instantaneous heat transfer distributions along centreline at t_S^* values (*a*) 0.0, (*b*) 0.13, (*c*) 0.23, (*d*) 0.40, (*e*) 0.53, (*f*) 1.0. Solid line: reference fully laminar flow. Small cross symbols and dot-dashed line: centreline data for fully turbulent wedge with inception at $x_S^* \approx -4.5$.

$x_S^* = 0$, and finally $\approx 6.8L_S$ when the back reaches $x_S^* = 1$ to complete transit. This spot transit time, τ_{tr} – that is, the time interval between the front reaching $x_S^* = 0$ and the back reaching $x_S^* = 1$ – is ≈0.185 ms or $\tau_{tr}U_e/\delta_0 \approx 124$. This is used to normalise time as $t_S^* = t/\tau_{tr}$ from here onwards, and was also used in figures 5 and 6.

The average front U_f and back U_b velocities (taken from the slope of the *x*–*t* trajectories) are 76 % and 34 % of the boundary layer edge velocity U_e, compared with 81 % and 40 % recorded well downstream at 332.5 mm $\leq x \leq$ 520 mm in Fiala *et al.* (2006). Figure 6(*d*) also includes the *x*–*t* trajectory for the axial position of maximum measured heat transfer for the spot. This is taken solely from the axial array, so it uses centreline data only, and higher values probably can be achieved off-centre. It also includes the trajectory for the axial location of the maximum width position. This is inferred from separate tests using the transverse array reported later. These data indicate that the axial position of maximum width occurs slightly behind the position of maximum centreline heat transfer.

Figure 7 presents centreline snapshots at different times, with $t_S^* = 0$ defined by the instant when the front reaches $x_S^* = 0$. Each snapshot comprises ten individual spots. Figure 8 presents the corresponding ensemble averages. The 64-sensor axial array was not long enough to capture a complete spot instantaneously, but the progressive motion of the front, peak heating and back region is clear. Again, the scatter in part reflects sampling errors and repeatability, while later times accentuate the effect of any length variations by virtue of the time-zero definition set by the arrival of the spot front. The figures also include data using a 120 μm height element at $x_k = 38$ mm to produce a *fully turbulent wedge* with the same effective origin at $x_S^* = -4.5$ as for the average isolated spot. Data points for the wedge are restricted to $x_S^* \leq 0.5$, but the data average line is extrapolated downstream. The closeness between spot peak heating rates and the turbulent wedge

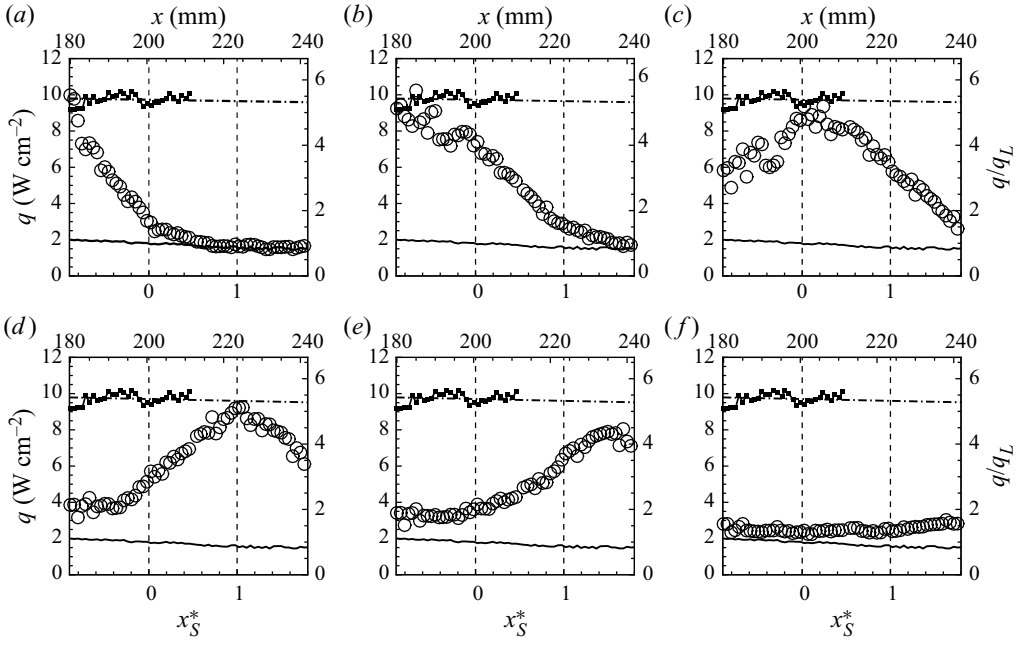

Figure 8. Ensemble averaged version of figure 7, with the same legend. Sample times correspond, using figure 6(*d*), to (*a*) front at $x_S^* = 0$, (*b*) front at $x_S^* = 1.0$, (*c*) q_{max} at $x_S^* = 0.08$, (*d*) q_{max} at $x_S^* = 1.04$, (*e*) maximum width at $x_S^* = 1.0$, (*f*) base at $x_S^* = 1.0$.

heating rates anticipates the consistency between isolated spots, amalgamating trains and fully turbulent wedges shown in figure 9. Ensemble-averaging the data emphasises the fact that the influence of the spot extends a significant distance beyond the location of the 1.6 factor threshold. A particular example is figure 8(*a*), where the nominal front (threshold factor defined) is at $x_S^* = 0$, whereas the actual influence extends at least a further 0.5 units in x_S^*. How much this represents actual presence of the turbulent disturbance or is a precursor laminar influence is difficult to judge.

4.3. *No-flare case: definition of incident spot characteristics in transverse direction*

Figure 9 shows two sample contours in the (z_S^*, t_S^*)-plane at $x_S^* = 0.2$ together with the corresponding spot width and centreline heat transfer histories. In figures 9(*a*,*c*), two isolated spots with fronts detected at $t_S^* = 2.9, 4.7$ are preceded by a triple event coalescence for $0 \leq t_S^* \leq 2.5$. Figures 9(*b*,*d*) show three isolated events and one large accumulation in progress. Figures 9(*c*,*d*) also include the histories of the spot 'part-width', that is, the distances from the centreline to the measured $\pm z_S^*$ edges. The differences in scale between the two sides for the isolated spots in these two sequences are characteristic of all isolated spots. That is a maximum difference of about $\pm 10\,\%$ with no apparent bias towards one side or the other, confirming that on average, spots follow the centreline downstream of the element.

Figures 10(*a*,*b*) show the dependence of maximum spot width and maximum centreline heat transfer rate, both at $x_S^* = 0.2$, on the normalised transit time (i.e. elapsed time between front and back reaching this position). This includes both isolated spots and amalgamating sequences. For amalgamations, the maxima rarely lie outside the range found for isolated spots. The few large excursions in width seem to be associated with an

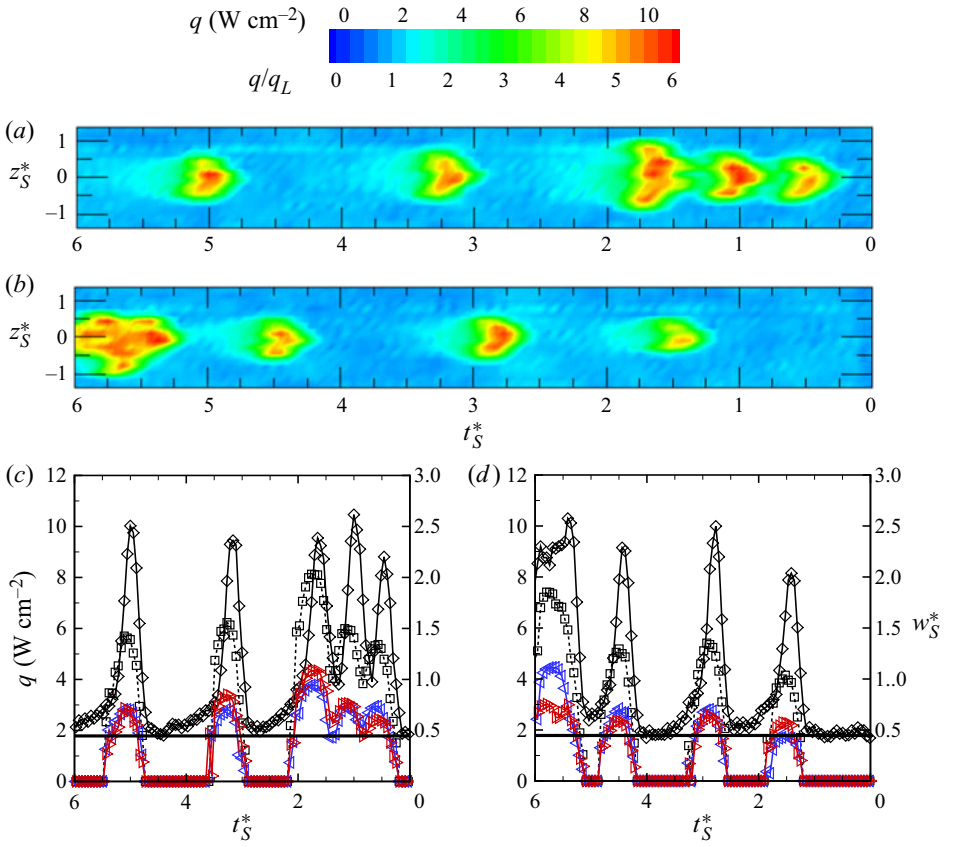

Figure 9. No-flare case. (*a*,*b*) Sample heat transfer contours in the (t_S^*, z_S^*)-plane at $x_S^* = 0.2$. (*c*,*d*) Corresponding time histories at $x_S^* = 0.2$: ◇, centreline heat transfer with solid line showing fully laminar reference value; □, spot transverse width normalised by L_S (w_S^*); ◁, part width from centreline to spot negative z_S^* edge; ▷, part width from centreline to spot positive z_S^* edge.

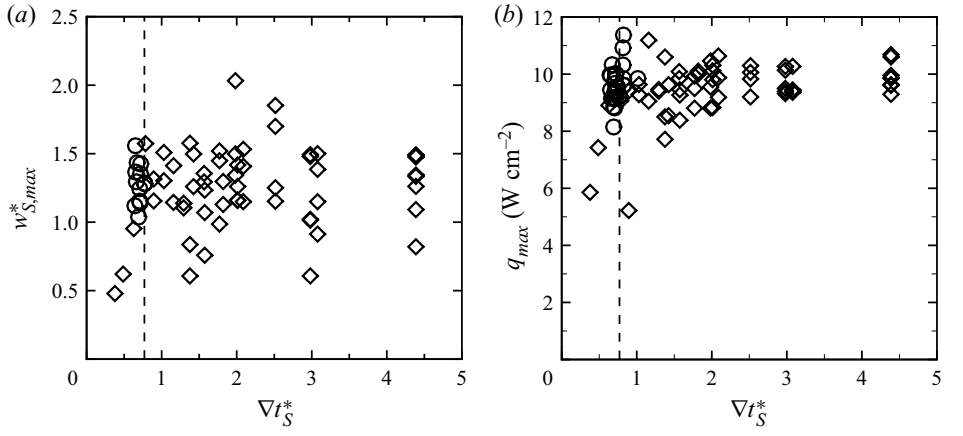

Figure 10. No-flare case. Transverse data at $x_S^* = 0.2$. (*a*) Spot normalised (by L_S) maximum width, $w_{S,max}^*$, versus normalised transit time at this position, ∇t_S^*. (*b*) Centreline heat transfer maximum q_{max}. Isolated spots, ○; coalescing spots, ◇; dashed line, time scale for average isolated spot transit through $x_S^* = 0.2$ taken from figure 7.

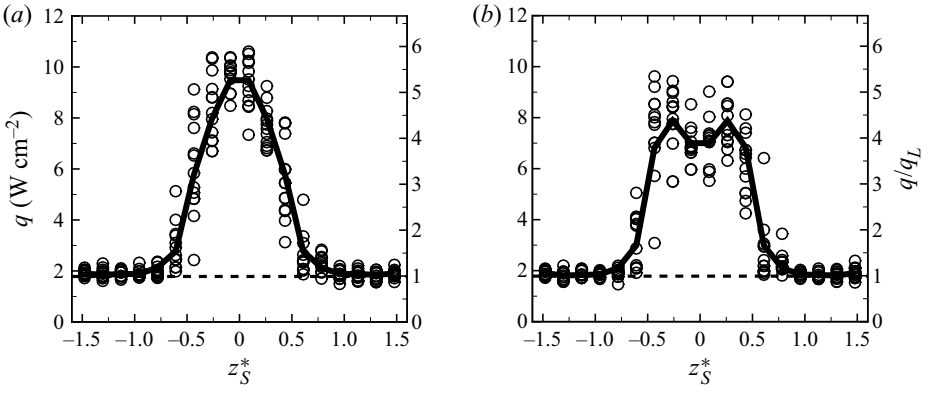

Figure 11. No-flare case. Transverse profiles of heat transfer, for isolated spots, at $x_S^* = 0.2$ at (*a*) instant of centreline heat transfer maximum q_{max}, and (*b*) instant of maximum width $w_{S,max}^*$. Solid line, averaged data; dashed line, reference laminar level.

'overtaking' tendency during the core–core interaction. For isolated spots, figures 9(*c*,*d*) show that the heat transfer maximum occurs before arrival of the maximum width position. From all data sets, the estimated x_S^*–t_S^* trajectory for the maximum width position is included in figure 6(*d*). This figure, together with figure 7(*a*), provides a ratio of spot length to maximum width of 3.25, with the maximum width position at approximately 65 % of the spot length.

Figure 11 presents ensemble and averaged transverse profiles of heat transfer at the instants of peak heating (figure 11*a*) and maximum width (figure 11*b*). The ensemble averaging 'reflects' data values about the centreline. For the maximum width position, slight heat transfer increases occur off-centreline, as seen near $z_S^* = \pm 0.25$. These are characteristic of cellular structures that appear in developed spots (figure 1), but the gauge scale in this study is too large, relative to w_S^*, to resolve these in more detail. From the derived inception location, the core and outer (edge) spreading half-angles appear effectively the same as for the fully coalesced (turbulent wedge) condition, $\alpha_c = 4.6^\circ \pm 0.9^\circ$ and $\alpha_e = 6.9^\circ \pm 1^\circ$. As shown in Fiala *et al.* (2014), these are respectively within the mid/low and upper bounds of the range of turbulent jet spreading rates expected from classic literature (Fischer 1972).

5. Flare case: turbulent spot impingement on initially laminar separation

5.1. *Initial visualisation of the transit of separation by single spots and trains of spots*

The transit of separation by turbulent spots is complex. A first impression of the main features is given in figure 12, which presents sample heat transfer contours in the (t_S^*, x_S^*)-plane for transit by both isolated spots and multiple spot events. Specific contour lines are shown in black, corresponding to the reference steady laminar separation and reattachment values taken from figure 3(*b*). These are highlighted as q_S and q_R in figure 12(*a*). These confirm that there are long periods when these have asymptoted to the no-roughness laminar separation and reattachment positions $x_S^* = 0$ and $x_S^* = 1$, for example, $17 \leq t_S^* \leq 26$ in figure 12(*b*). It also so happens that for the reference case of figure 3(*b*), the heat transfer at $x_S^* \approx 0.62$ is the same as the separation value. That segment of the contour line in figures 12(*a*,*b*) therefore has no specific meaning, apart from the recognition that it too asymptotes to its correct spatial position. Two clear isolated spots

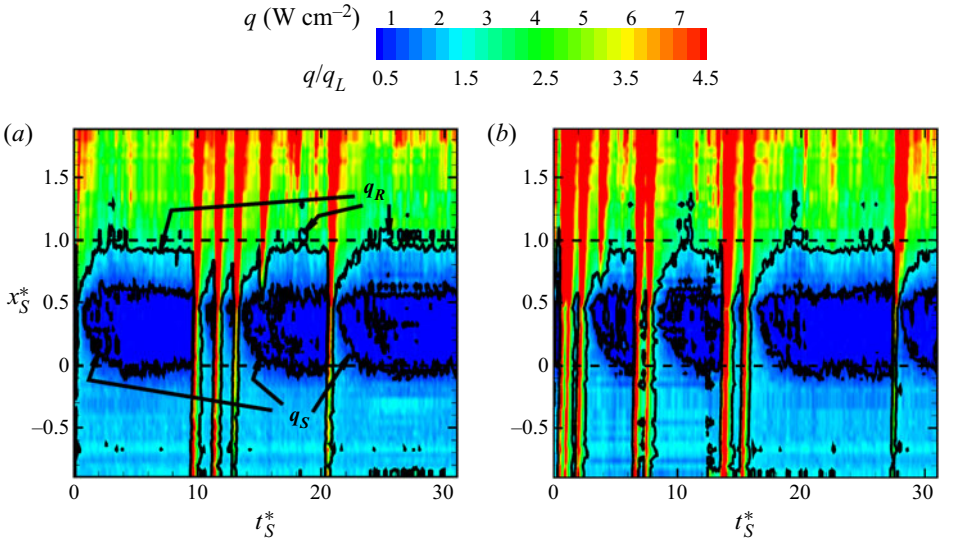

Figure 12. Flare case with roughness-induced turbulent spots, axial heat transfer sensor array. Heat transfer contours in the (t_S^*, x_S^*)-plane for two sample runs. Solid black lines are isolines at reference separation and reattachment levels taken from figure 3(*b*); for clarity these are denoted as q_S and q_R, respectively in (*a*). Horizontal dashed lines highlight the reference $x_S^* = (0, 1)$ locations.

are seen in these figures, at $t_S^* \approx 20.5$ in figure 12(*a*) and at $t_S^* \approx 28.0$ in figure 12(*b*). The triple spot packet in figure 12(*a*), for $9 \leq t_S^* \leq 14$, is joined by a fourth event, $t_S^* \approx 14.0$, but becoming apparent only at $x_S^* \geq 0.6$. Downstream of $x_S^* \geq 1.0$, further high heat transfer streaks appear in both figures. This was not evident in the reference no-roughness case and is indicative that the presence of spots and/or roughness element wakes further destabilises the reattaching flows.

5.2. *Flare case: heat transfer histories at various axial stations*

The isolated spot time-histories for the flare case, at selected axial stations on the centreline, are presented in figure 13. Again, $t_S^* = 0$ is taken as the instant of peak heating. Figure 14 presents the corresponding ensemble averages. Each figure starts and returns to the reference laminar separation state after approaching close to, or slightly exceeding, the reference (attached) turbulent wedge level. This indicates the local collapse of separation accompanied by a transient period of attached turbulent flow, followed by relaminarisation and reseparation. Figures 13(*a*) and 14(*a*) are far enough upstream ($x_S^* = -0.5$) to be unaffected by separation, and the histories are essentially identical to the no-flare case. The sensor location in figures 13(*b*) and 14(*b*) is $x_S^* = -0.15$. This is still in the attached flow region for the reference flow, slightly upstream of separation. Nonetheless, it is in the precursor influence of separation, which figure 3(*b*) indicates to extend upstream at least of order 0.3 in x_S^*. The full recovery times are now much extended, of order 4 units in t_S^* after the peak. In fact, the heat transfer fall from the peak establishes at an intermediary plateau, close to the value for the laminar no-flare case. This suggests that the flow locally has now relaminarised, but that although separation will be re-establishing at the cylinder–flare junction, and progressively growing in scale upstream and downstream, its upstream precursor influence does not yet extend as far as the sensor location. Only after $t_S^* \approx 2.25$ does the heat transfer recommence its fall to its final state. Moving slightly downstream

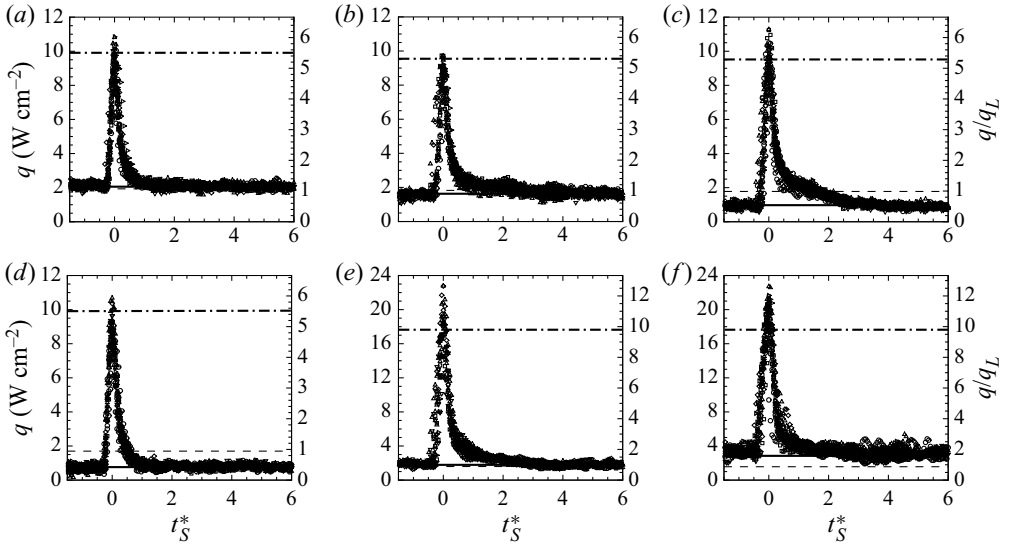

Figure 13. Flare case. Heat transfer time-histories for isolated spots at various axial stations, (*a–f*) $x_S^* = -0.50, -0.15, 0.02, 0.46, 0.76, 1.02$. Solid line, reference laminar flare case; dashed line, reference laminar no-flare case; dashed-dot line, reference turbulent wedge; $t_S^* = 0$ is referenced at time of maximum heat transfer.

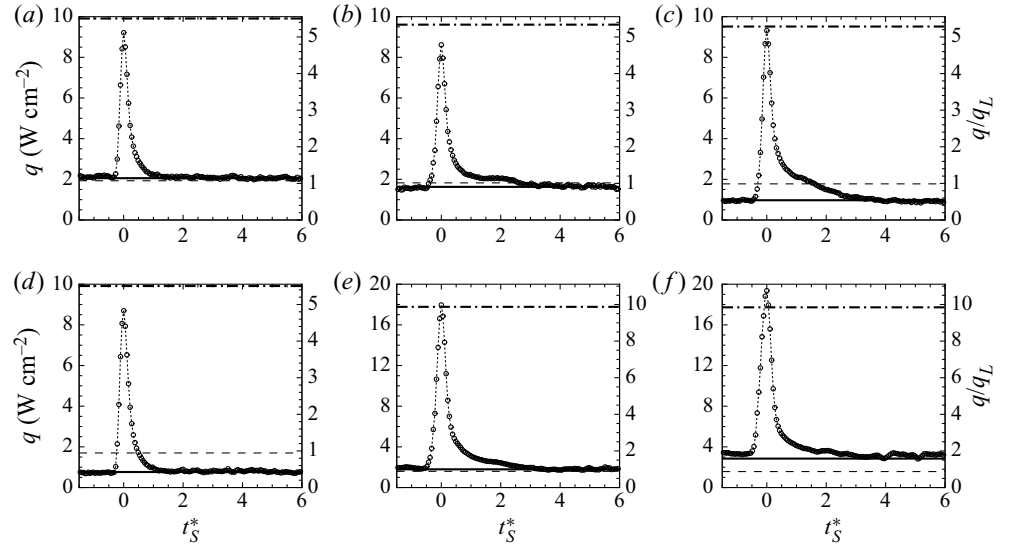

Figure 14. Ensemble average version of figure 13.

to $x_S^* = 0.02$, figures 13(*c*) and 14(*c*) show that a residual effect is still apparent as an inflexion in the profile. Closer to the cylinder–flare junction, the recovery time is the most rapid, seen in figures 13(*d*) and 14(*d*) for $x_S^* = 0.46$. It then increases again with downstream distance in figures 13(*e*,*f*) and 14(*e*,*f*), presumably similar in mechanism to the stations near separation. This would imply that there is a transitory period when an attached laminar flow establishes on the flare before the downstream movement of the reattachment zone sweeps over it. Despite the apparent differences in establishment

behaviour, for these various axial stations, in a separated flow all positions ultimately can asymptote only to their fully established states at the same time.

5.3. *Flare case: isolated spot transit and axial distributions of heat transfer*

Figure 15 presents the ensemble average spatial distributions along the centreline, at specific sample times, for the isolated spot interaction. Each subfigure represents the averaging, at a specific sample time, of nine individual records. The time t_S^* is set at zero when the advancing spot first achieves the 1.6 factor threshold at $x_S^* = 0$. For comparison, the subfigures include: the equivalent ensemble averages for the no-flare case; the reference laminar data for the flare and no-flare cases; and the turbulent wedge data for the flare case.

The subfigures reveal many important features of the interaction.

(1) Pre-transit (figure 15*a*) and post-transit (figure 15*l*) distributions match the reference laminar case closely through the separation region, $0.0 \leq x_S^* \leq 1.0$, and upstream as far as the first sign of the approaching spot at $x_S^* = -0.6$ in (figure 15*a*). Downstream of $x_S^* = 1.0$, however, the distributions in figures 15(*a*) and 15(*l*) are all above the laminar reference measurements, which themselves were above the laminar CFD (figure 3*b*). In particular, figure 3(*b*) showed a local measured maximum at $x_S^* \approx 1.4$, after which it clearly fell towards the laminar CFD level. In contrast, figures 15(*a*,*l*) indicate no such behaviour, with the difference between the roughness and no-roughness cases increasing steadily with axial distance. This difference is still very small compared with the heating levels on the flare for the full turbulent wedge case ($q/q_L \approx 9.0$), shown for comparison, but is probably indicative that with the presence of a roughness element, and the wakes of preceding isolated spots and the possible presence of streamwise structures, transitional disturbances are developing at reattachment and downstream.

(2) A significant point from figure 15(*c*) is that although there is a clear perturbation from the reference state for $x_S^* \leq 0.5$, the separation zone is barely altered downstream of this position. This is consistent with the speed of spot advance exceeding that of any internal disturbance propagation within separation.

(3) For figures 15(*d*–*j*) (until reseparation starts, by figures 15*h*,*i*), the closeness of the averaged no-flare and flare distributions upstream of the junction suggests that the spot is little affected by the interaction and that the (centreline) separation has therefore nearly, or fully, collapsed. Downstream of the junction, although the no-flare/flare levels clearly must be different, the close correspondence of the positions of maximum spot heating (figures 15*f*–*i*) again emphasise the relative insensitivity of the spot to the interaction.

(4) Figures 15(*f*–*i*) show distinct step increases at the junction corresponding to the establishment and growth of an attached shock. The mechanism for this shock formation will be considered further in § 6.

(5) Downstream of $x_S^* \approx 0.5$ in this attached shock phase, the distribution everywhere sits well above the reference laminar value with the peak heating asymptoting to the turbulent wedge data, so that this flow is almost certainly fully attached. Judging when reseparation starts is difficult, but it probably occurs before full laminar recovery. An indicator for laminar separation, certainly for steady flows and maybe for the slow re-establishment here, is a heat transfer reduction as separation is passed. This is clear in figures 15(*j*,*k*), with a hint of a reduction already in figure 15(*i*).

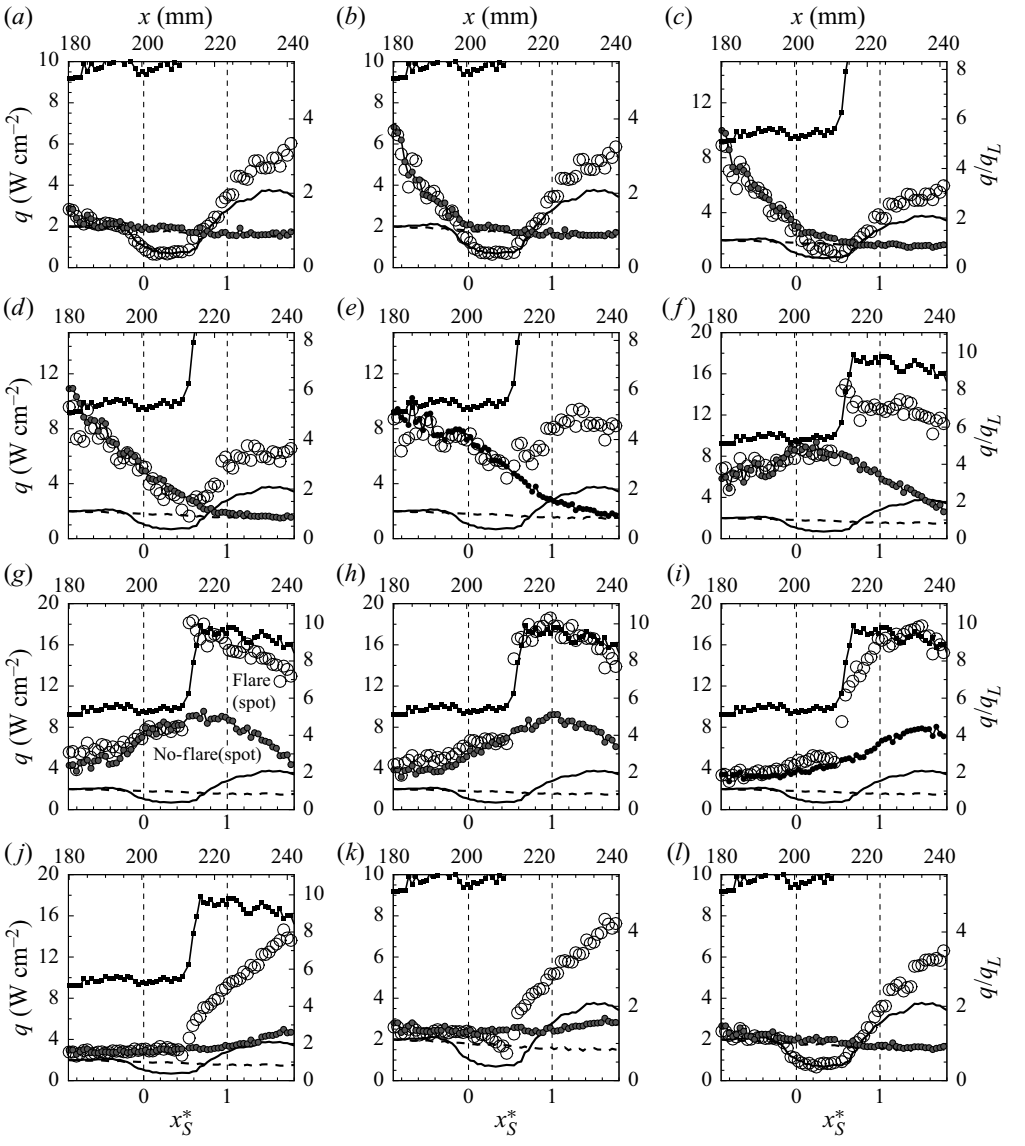

Figure 15. Flare case. Ensemble average axial profiles at selected times for isolated spot transit of separation. ○, spot transit data at time t_S^* values (*a*) −0.20, (*b*) −0.065, (*c*) 0.0, (*d*) 0.065, (*e*) 0.13, (*f*) 0.23, (*g*) 0.32, (*h*) 0.40, (*i*) 0.53, (*j*) 0.72, (*k*) 1.0, (*l*) 2.8. ●/solid line, comparative data for average no-flare isolated spot; ■/solid line, turbulent wedge flare data; solid line, laminar separation (flare); long dashed line, laminar attached boundary layer (no flare).

5.4. *Flare case: isolated spot transverse distributions of heat transfer*

Figure 16 presents ensemble and averaged transverse profiles of heat transfer at $x_S^* = 0.2$ at the times when the spot reaches its peak heating position at the centreline (figure 16*a*) and, slightly later, at the instant of maximum spot width (figure 16*b*). It includes the corresponding average no-flare data (from figure 11). Because of the inevitable fluctuation in heat transfer signals, in the outer intermittent region of the turbulent spot, and the fact that edge detection means that the assessment is made simultaneously from multiple gauges, determination of the instant of maximum width is more prone to error than

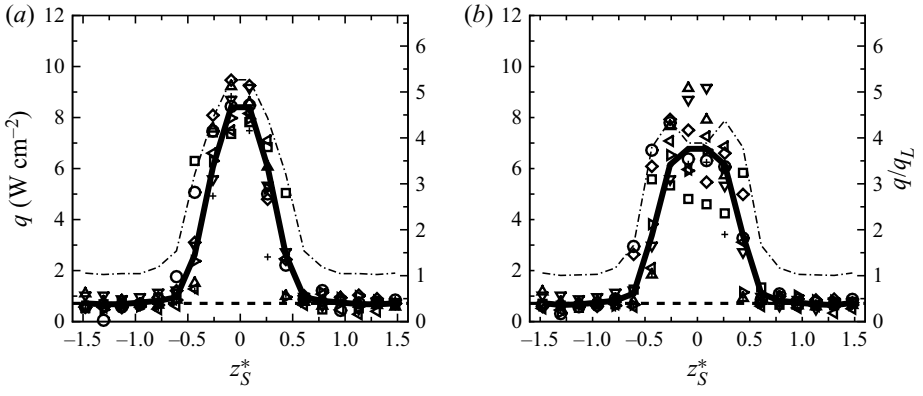

Figure 16. Flare case. Transverse heat transfer profiles for isolated spots at $x_S^* = 0.2$ at the instants of (*a*) centreline maximum heat transfer and (*b*) maximum spot width. Solid line, averaged data; dashed line, reference laminar separation; dashed-dot line, average no-flare data.

detecting the instant of maximum centreline heating. For this reason, transverse profiles show more scatter for the maximum width case than for maximum heating. This applies equally to the no-flare (figure 11) and present flare cases. Flare and no-flare data are also clearly affected by the different asymptotic heat transfer levels for large z_S^*, which influences the perception of width. Nonetheless, the flare case suggests a slightly narrower width. For example, taking the maximum heat transfer mean profiles (figures 16*a* and 11*a*), and determining a width corresponding to a heat transfer level at 25 % of the interval from minimum to maximum, gives a no-flare width of 1.09 units in z_S^* and a flare width of 0.89. One potential contribution is that this is consistent with the development of unsteady wave interactions, and resultant slight inward cross-flow velocities, as the spot moves through the separation zone. These are discussed in § 6, amounting to an estimated inflow $\approx$3 % U_e or a potential contribution of $\approx$16 % in width reduction.

6. Wave interactions and 3-D flow physics for the separation collapse

6.1. *Spot initiation wave system*

When the spot forms, initially an unsteady 'starting wave' system (*SW*) is produced. An idealisation of this in the (x_S^*, y_S^*)-centreplane is shown in figure 17(*a*). This corresponds to the instant when the apex of the average spot, initiated at $x_S^* \approx -4.5$, reaches $x_S^* = -0.5$. *SW* is approximated as a hemispherical acoustic wave whose effective centre travels at the boundary layer edge velocity. The external flow is faster than the spot, and from the mean base and front speeds (table 4), relative Mach numbers are supersonic at the base ($\approx$2.26), supporting a swept 'base wave' system (*BW*) represented by a Mach wave, and subsonic ($\approx$0.86) at the apex.

The separation and reattachment shock waves are denoted as *SS* and *RS*, and although the leading segment of *SW* has passed well downstream of reattachment, *SS* and *RS* are not expected to experience any detectable perturbation from it. A schlieren snapshot in figure 17(*b*), for the passage of a spot in the no-flare case, indicates a swept wave, presumed to be a spot-induced *BW* though barely any resolution of the spot itself is possible. The wave angle $\approx$34.5° is larger than that for the idealisation ($\approx$27°), indicating a lower relative Mach number (1.76 versus 2.26). This difference is partly within the margins for base speed variations for individual spots, and might also indicate that the wave originates not at

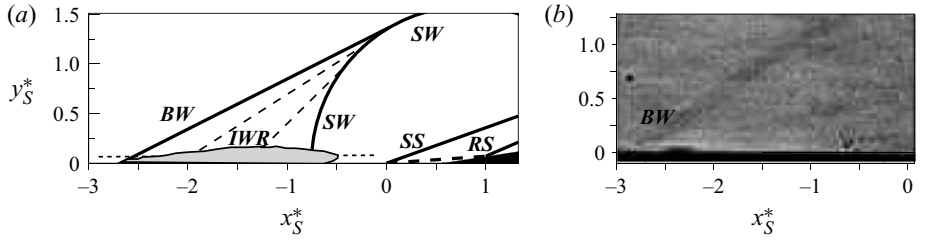

Figure 17. (*a*) Idealised schematic for the centreline weak wave system, generated by a spot formed initially at $x^*_{S,o} \approx -4.5$, at the instant that its apex reaches $x^*_{S,apex} = -0.5$. *SW*, starting wave formed at spot inception; *BW*, swept wave formed at base of spot; *IWR*, intermediary Mach waves; *SS* and *RS*, separation and reattachment shocks, respectively; fine dashed line, reference edge position for approach laminar boundary layer. (*b*) Schlieren snapshot of spot with base wave at $x^*_{S,base} \approx -3.0$ for the no-flare case.

L_S/δ_0	U_f/U_e	U_b/U_e	L_0/L_S	L_0/W_0	α_c	α_e	τ_{tr} (ms)	$\tau_{tr}U_e/\delta_0$
12.2	0.76	0.34	2.5	2.3	4.6°	6.9°	0.185	124

Table 4. Key interaction properties, including the ratio of separation length to boundary layer thickness L_S/δ_0 and no-flare spot average data taken with spot apex at $x^*_{S,apex} = 0.0$ ($t^*_S = 0$). Spot data include: spot front and back velocities normalised by edge velocity, U_f/U_e and U_b/U_e; spot length normalised by separation length L_0/L_S and by spot width L_0/W_0; core and outer (edge) spreading half-angles, α_c and α_e; and the transit time τ_{tr} between spot apex reaching separation and base reaching reattachment.

the base position, as defined by the surface heat transfer threshold, but further downstream in the intermediary wave region *IWR* indicated in figure 17(*a*).

6.2. *Wave system as spot enters separation region*

The centreline heat transfer data have been used to infer details such as separation collapse and the formation of the cylinder–flare junction shock. However this gives limited insight into the 3-D mechanisms involved. This is explored further by introducing pressure and schlieren data in § 6.3 and developing here a simple model for the unsteady wave physics. It is not restricted to the specific conditions of this study although it is dependent on the fact that the spot length is large compared with L_S. It also is appropriate for the case of a fully developed turbulent wedge impinging on separation.

As the spot penetrates the separation region, it produces an unsteady 3-D wave system driven by the pressure differences between the central collapsing-separation and the outboard, as yet undisturbed, separated zone. The spot planform is treated as a wedge whose semi-apex angle 14° matches the mean line from the apex to the maximum width. The spot height is assumed to be shallow compared with its planform scales. Waves are treated by a mix of acoustic and real shock angles, although waves are relatively weak anyway. It is assumed that locally the separation collapses immediately it encounters the apex and leading edges of the spot.

In figure 18, the spot apex has passed separation but not yet reached the cylinder–flare junction. Here the basic reference length scale is the length of spot that has entered separation; $\bar{X} = 0$ denotes the initial separation line, and $\bar{X} = 1$ the spot apex, and $\bar{Z}$ and $\bar{Y}$ denote the normalised circumferential and body normal distances.

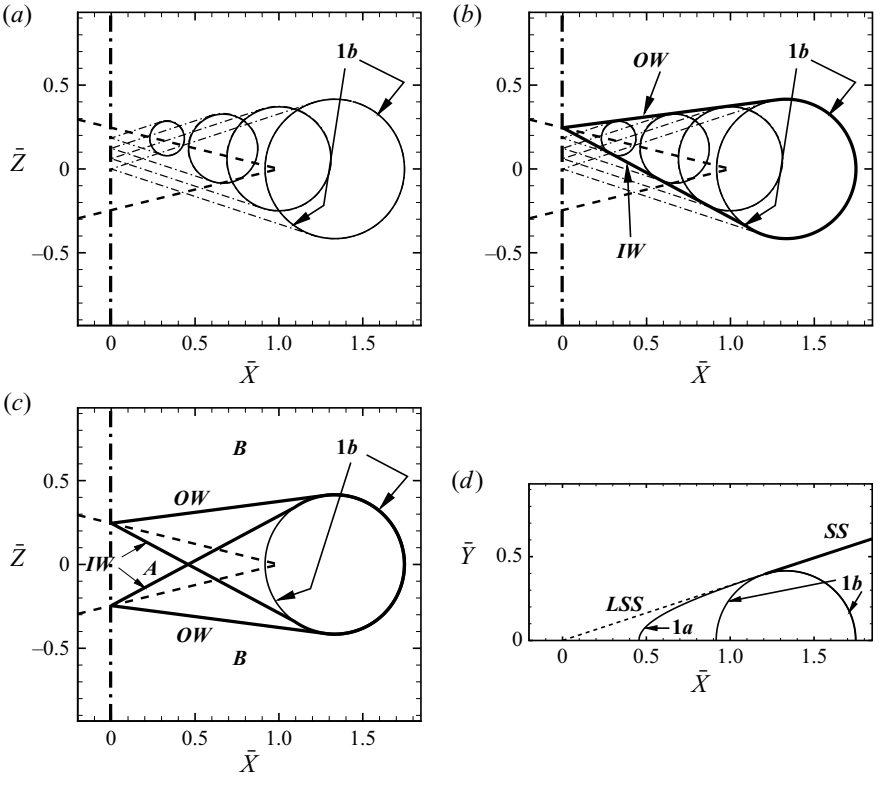

Figure 18. Schematic for simple wave interaction model, where $\bar{X}$, $\bar{Y}$, $\bar{Z}$ represent normalisation by the axial length of the spot segment that has passed separation. (*a–c*) Planform view in $(\bar{X}, \bar{Z})$-plane; dashed triangular shape denotes idealisation for spot planform. (*d*) View in centreplane, $(\bar{X}, \bar{Y})$, corresponding to (*c*). *SS*, separation shock; *LSS*, lost segment of separation shock.

Figure 18(*a*) shows the wave system, in planform (for $\bar{Z} \geq 0$ only), resulting from the first impingement of the spot apex on the separation line, together with waves initiated at various instants of the outwards sweep of the spot leading edge along the separation line. Each comprises a circular front (denoted as 1*b* for the foremost wave), propagating outwards at the local speed of sound relative to an effective centre travelling at the boundary layer edge velocity. Its downstream evolution is contained within two Mach lines. Although we assume that the separation region in figure 18(*a*) has collapsed everywhere under the spot, the surface pressure does not collapse simultaneously to attached flow values. The pressure zones are actually delineated by the wave fronts, *IW* and *OW* (inwards- and outwards-facing), shown in figures 18(*b*) and 18(*c*). The latter figure now includes the system for $\bar{Z} \leq 0$. Both *IW* and *OW* are translating outwards as the spot front sweeps along the separation line. The zone between *IW* and *OW* is unsteady. It is the accommodation zone between region *B*, as yet unaffected by the spot, and region *A*, where the pressure has collapsed to the attached flow value. At this stage, the pressure in zone *B* is higher than in zone *A*. This requires *IW* and *OW* to be compressive and expansive, respectively. Simultaneously, this also induces a weak inflow in the accommodation zone, assessed from unsteady wave modelling as $\approx$3 % of U_e. In reality, *IW* being compressive would be slightly less swept than indicated, and may be sufficiently strong to force a swept

separation in the unsteady zone between *IW* and *OW*; this would link to the separation in region *B* as part of the three-dimensionalisation of the separation zone.

The two 'wedge/circle' domains presented in figure 18(*c*) (i.e *OW*-1*b*-*IW*) correspond, off surface, to 'semi-cone/semi-sphere' regions. The main features in the $\bar{X}$–$\bar{Y}$ centreline symmetry plane are therefore as shown in figure 18(*d*). The first disturbance front 1*b* is highlighted again and the intersection line between the two semi-cones produces segment 1*a*. Upstream of 1*a*, the separation shock wave is lost on the centreline (and for some distance outboard), denoted as *LSS*, while downstream the separation shock wave segment *SS* is as yet unaffected.

Figure 19 continues this modelling when the spot apex has passed the cylinder–flare junction. Assuming that spot front/back speeds are little changed by the interaction, which is consistent with the heat transfer data of § 5.2, this occurs at $t_S^* \approx 0.065$ for the mean spot. The junction shock wave now initiates. It grows steadily in spanwise and streamwise extent, shown in figures 19(*a–d*) as wave 2*c*. The remaining system, 2*a* and 2*b* in figures 19(*a–d*), initiated by the spot apex passing the junction, has origin similar to 1*a* and 1*b* in figure 18(*d*). At this stage the conditions approaching the junction are still time-varying. Only when the apex of surface zone *A*, of figure 18(*c*), reaches the junction can steady conditions establish there. This occurs at $t_S^* \approx 0.14$. Wave 3*c*, in figures 19(*e*,*f*), shows the extent of junction shock formed by $t_S^* = 0.17$ and $t_S^* = 0.20$; features 3*a* and 3*b* again have origins similar to 1*a*/1*b* and 2*a*/2*b*.

The mechanism for loss of reattachment shock wave (*RS*) is difficult to prescribe although it must remain undisturbed until 1*b* reaches it. *RS* is represented in figure 19 by a solid line segment (as yet unaffected) and dashed line (disturbed). In reality, *RS* will assume a complex shape while it collapses and is swept downstream.

Finally, the spot base reaches separation at $t_S^* \approx 0.71$. The pressure differential between the outer separation zone and inner attached zone remains, providing a weak inflow velocity estimated earlier as $\approx 3\,\%\ U_e$. This would now contribute to channel closure together with the viscous recovery in the spot wake.

6.3. *Dynamic pressure and schlieren data: combined snapshot records of spot transit*

As well as the surface heat transfer data, dynamic surface pressure measurements were recorded along the axis together with schlieren visualisation. These are presented in figures 20–22, at significant snapshot times, together with corresponding pictures from the wave model.

The schlieren used a high-speed imaging system, visualising the (x_S^*, y_S^*)-plane. Picture quality is modest, resulting from factors including: there is transverse curvature of model and flow field; many significant waves are highly swept in the (x_S^*, z_S^*)-plane; the wave model indicates the overlap of many transient events; the test flow region was a 'confined free jet' downstream of the nozzle exit and the schlieren therefore also picks up turbulent fluctuations from the free jet boundary. The spot itself was not detectable by schlieren during the interaction, although figure 17(*b*) showed that it is visible potentially through its associated weak base wave system.

Pre-spot arrival at $t_S^* = -0.125$, the snapshot pressure distribution of figure 20(*d*) matches well with the reference steady data, both in the separation zone and also in the upstream/downstream attached flow regions. Heat transfer also agrees closely with the reference data for the separation region, $0.0 \leq x_S^* \leq 1.0$, but shows that already the spot causes a perturbation, from the reference laminar boundary layer, for $x_S^* \leq 0.0$. This was commented on previously as the inevitable difference between fronts defined by

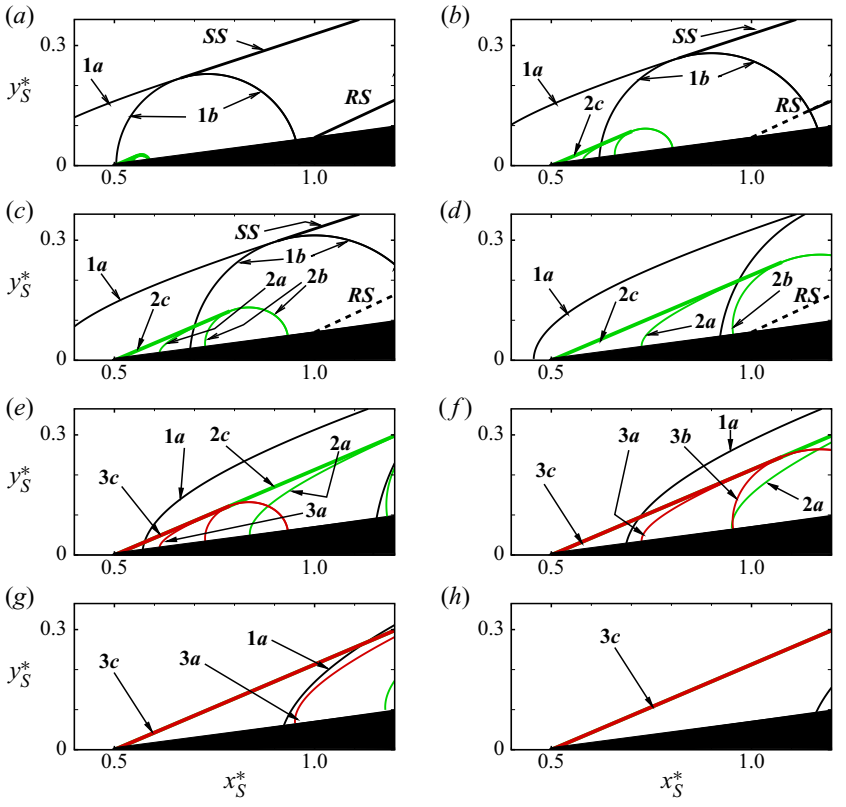

Figure 19. Schematic in the centreplane for the progressive loss of separation (*SS*) and reattachment (*RS*) shock waves, and the corresponding formation of an attached shock wave at the cylinder–flare junction (waves 2*c* and 3*c*). Panels (*a–h*) correspond to spot apex at $x_S^* = 0.55$, 0.675, 0.75, 1.0, 1.25, 1.5, 2.0 and 2.5 (with t_S^* values 0.07, 0.086, 0.10, 0.13, 0.17, 0.20, 0.26 and 0.32). Waves 1 (black), 2 (green) and 3 (red) are initiated respectively when (i) the spot apex reached the separation position, (ii) the spot apex reached the cylinder–flare junction, and (iii) the apex of region *A* in figure 18(*d*) reached the junction.

the 1.6 factor threshold and the actual first detectable disturbance. The idealised wave system for the separation/reattachment shock system is included (ignoring any boundary layer displacement effect) and guided by this, together with the reference case shown in figure 3(*c*), a two-shock system is just detectable in the schlieren. The same wave system is also seen at the end of the sequence in figures 22(*l*), together with the full re-establishment of the heat transfer distribution for $x_S^* \leq 1.0$ and the near, but not complete, recovery in pressure.

The two-wave system of figure 20(*g*) changes to a single front in the schlieren of figure 20(*i*), and the transition to this is just evident in the schlieren of figure 20(*h*) as well. Although figure 20(*i*) is not sharp, it shows a front with a clear convex (upwards) curvature. This is consistent with the wave model. It therefore is probably a combination of the intersection line 1*a*, defined in figure 19(*e*), together with the preliminary stages of formation of the junction attached shock wave (2*c*/3*c*). Shock formation is also evident in the step increases in heat transfer and pressure at the junction, starting with figures 20(*b*,*e*). The pressure, for $x_S^* \leq 0.5$, possibly suggests a modest reduction in axial separation scales rather than a complete or near collapse. It also shows a significant fall in axial pressure gradient, just downstream of the junction, which is an effect that persists at

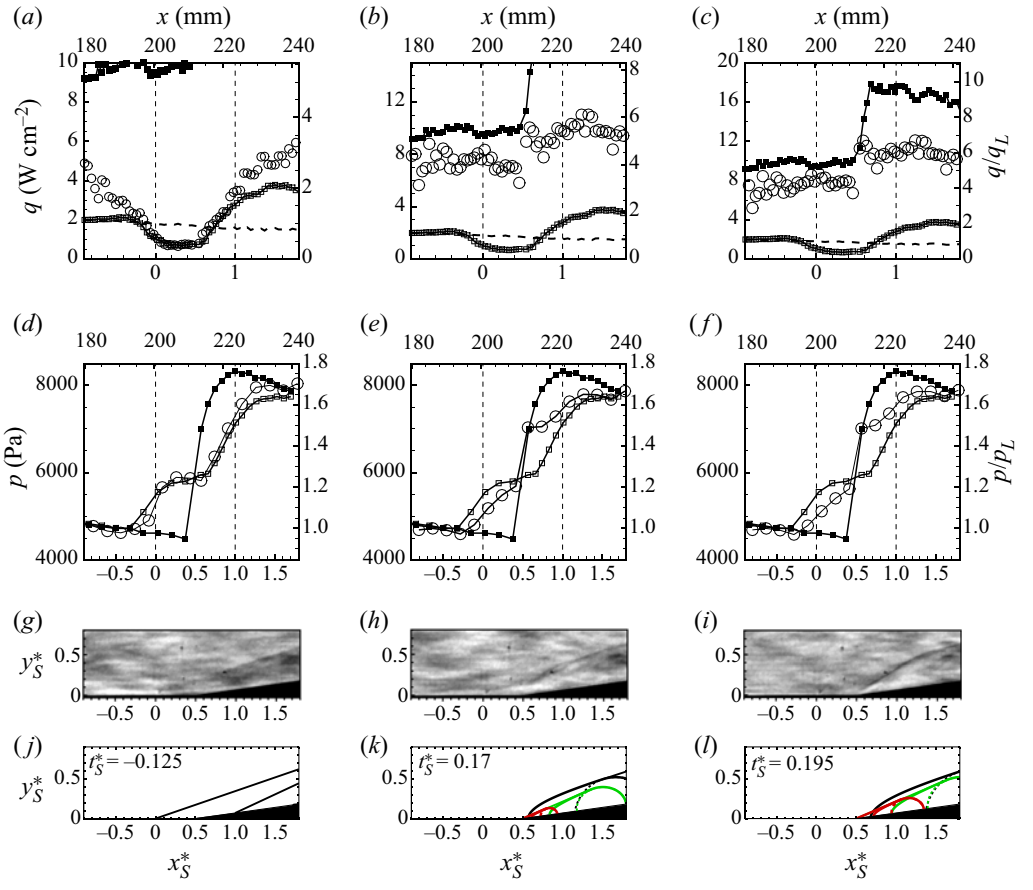

Figure 20. Snapshot data for flare configuration taken at the times specified for each column. Panels (*a–c*) heat transfer, and (*d–f*) pressure, use: open circle, ensemble average data for isolated spots; open square, reference laminar data; solid square, reference turbulent wedge data; dashed line, reference laminar no-flare data. (*g–i*) Schlieren. (*j–l*) Proposed wave system in centreline plane according to § 6.2. Data taken at following times: (*a*,*d*,*g*,*j*) $t_S^* = -0.125$ with spot apex at $x_S^* \approx -0.9$; (*b*,*e*,*h*,*k*) $t_S^* = 0.17$ with spot apex at $x_S^* \approx 1.33$; (*c*,*f*,*i*,*l*) $t_S^* = 0.195$ with spot apex at $x_S^* \approx 1.5$.

least until figure 21(*d*). However, this could be explained by figure 19, which suggests that during this period the intersection line 1*a* still lies in the range $0.5 \leq x_S^* \leq 1.0$, so that the flare centreline potentially is still located in the combined fields of the two 'semi-cone/semi-sphere' regions.

The step increases in heat transfer and pressure at the junction, together with the schlieren and wave model, show the dominance of the junction shock wave for all three sample times in figure 21. The sequence of schlieren, in figures 21(*g–i*), indicates a slight progressive lowering of the height of the junction shock. This might simply show, for example, displacement effects of the boundary layer and spot. In addition, the wave model sequence suggests that the intersection line 1*a* (in black) still elevates itself slightly above the level of the corner shock (in red) at $t_S^* = 0.27$ (figure 21*j*), with progressively less influence as it travels downstream in figures 21(*k*) and 21(*l*).

The pressure distribution reaches its most collapsed state in figures 21(*f*) and 22*d*). In this interval, the spot maximum width position passes $x_S^* = 1.0$ and the base has

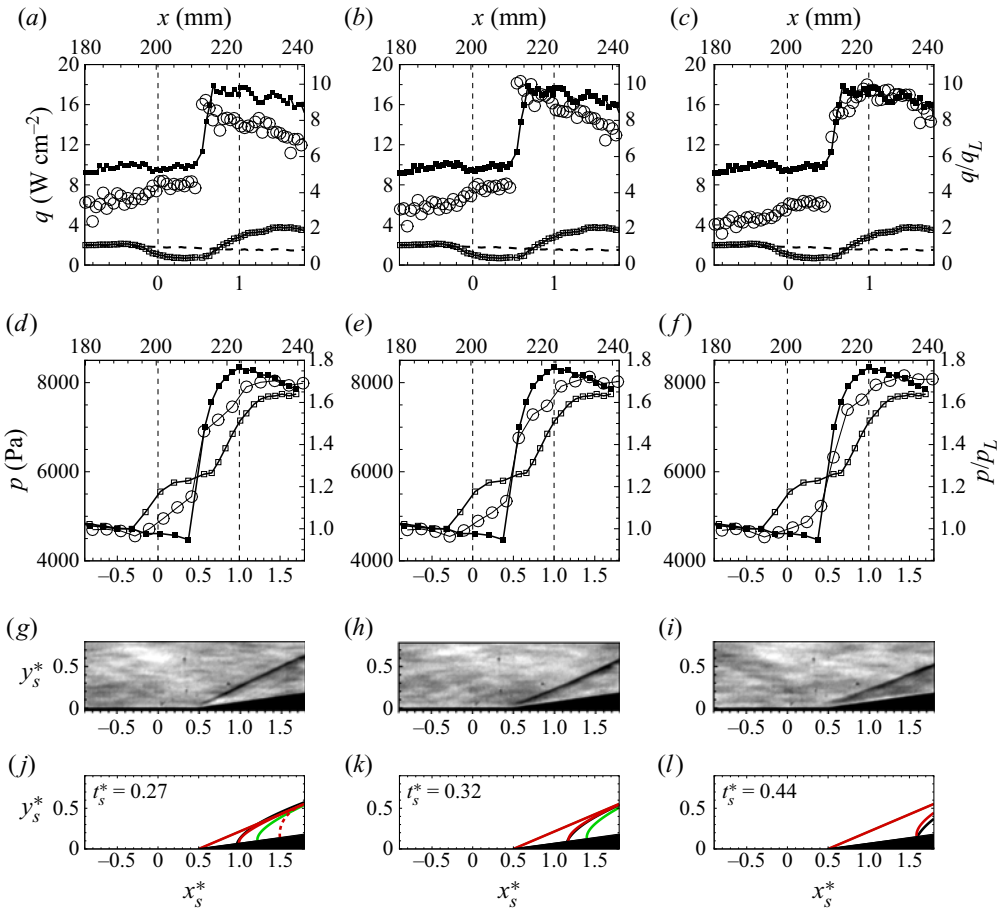

Figure 21. Legend as for figure 20. (a,d,g,j) $t_S^* = 0.27$ with spot apex at $x_S^* \approx 2.1$ and spot maximum width at $x_S^* \approx -0.33$. (b,e,h,k) $t_S^* = 0.32$ with spot apex at $x_S^* \approx 2.5$, maximum width at $x_S^* \approx -0.08$ and base at $x_S^* \approx -1.38$. (c,f,i,l) $t_S^* = 0.44$ with maximum width at $x_S^* \approx 0.5$ and base at $x_S^* \approx -0.96$.

passed $x_S^* = 0$. The pressure distribution does not achieve the same abrupt step at the junction as does the distribution for the fully turbulent wedge, which shows no precursor upstream influence at the junction. However, comparison with a turbulent state is not fully appropriate anyway. Between the two figures, the heat transfer falls from a high level, probably turbulent, to essentially laminar levels (figure 22a), with a very slight dip at the junction as an indicator that reseparation has started. The developing fuzziness near the wall, in the schlieren, probably indicates the initiation of a compression fan at the junction that will evolve into separation and reattachment shocks. In figures 22(j,k), no wave model is presented because it does not cover the recovery phase.

7. Concluding remarks

A body of revolution avoids issues with lateral end effects that can be problematic for planar geometries, but this does not guarantee an axisymmetric reference flow, as illustrated by visualisation of streamwise structures in the vicinity of reattachment. The evidence, however, is that these are generally characteristic of separated flows rather

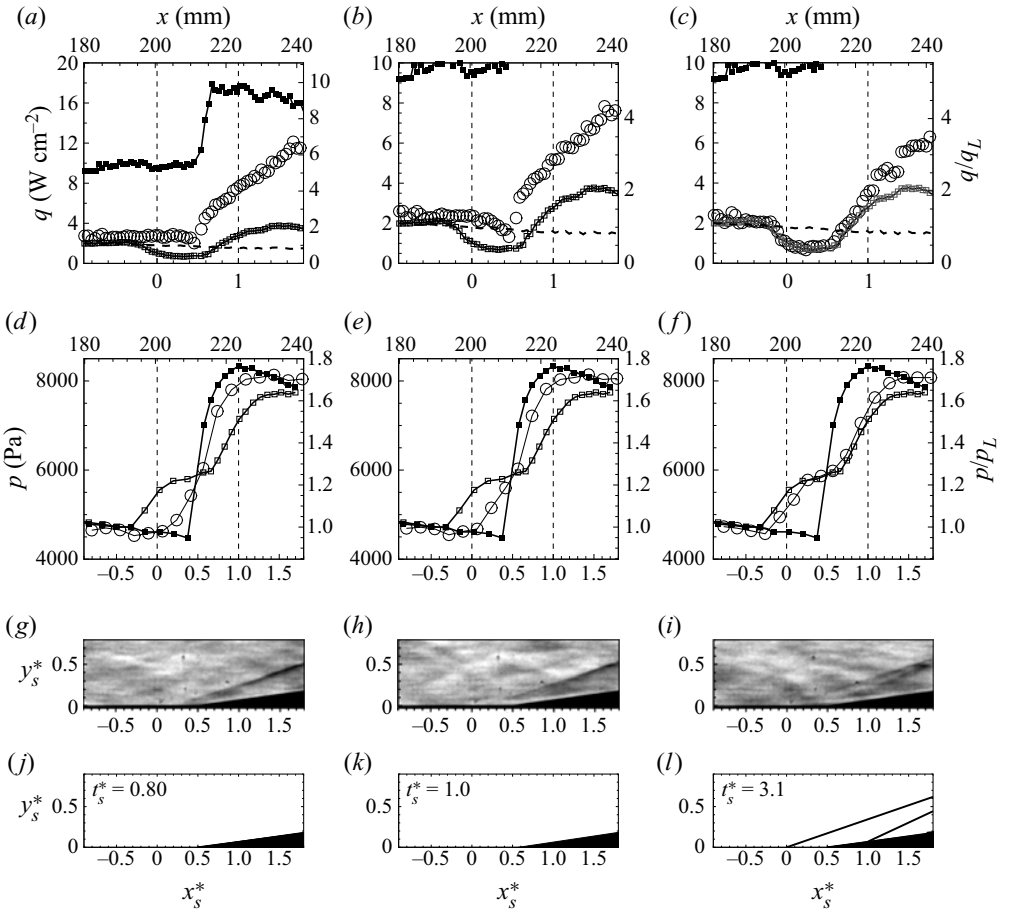

Figure 22. Legend as for figure 20. (a,d,g,j) $t_S^* = 0.80$ with spot maximum width at $x_S^* \approx 2.3$ and base at $x_S^* \approx 0.3$. (b,e,h,k) $t_S^* = 1.0$ with spot base at $x_S^* \approx 1.0$. (c,f,i,l) $t_S^* = 3.1$.

than specific to the present geometry. The circumference of the body, and hence the circumferential span of the separation, is 10.25 times the separation length L_S. Given the large time scale for circumferential propagation of disturbances, the finite span can be deemed to effectively have no influence during the interaction.

Boundary layer transition is induced by a single roughness element on the nose, with element height set close above critical conditions to produce isolated spots. The basic reference time scale τ_{tr} taken for the isolated spot is the total transit time between the spot apex first reaching separation and the base reaching reattachment, giving on average $\tau_{tr}U_e/L_S \approx 10.1$. This is essentially a convective time scale, although it includes the growth of the spot during the interaction when it more than doubles its length and width. The separation re-establishment time is approximately $4\tau_{tr}$, so that spot spacing has to be large to truly isolate their effect. This requires centreline turbulent intermittency levels less than 15 % when the spot front reaches separation.

The spot provides a large perturbation, with its large-scale structure only mildly altered, whereas the separation is totally collapsed in the interaction zone. Collapse is rapid, but progressive, during transit. Given the high speed of the spot advance, which is greater than disturbance propagation speeds within the separation, the downstream part of separation

can be unaffected while the upstream part may effectively be fully collapsed. The precursor disturbance, travelling downstream outside the free shear layer, clearly precedes the spot apex but appears to have little detectable effect on separation collapse. Re-establishment of full separation is much slower and is driven by two effects: the slow inwards closure of the 'channel' formed by the initial separation collapse, after the spot base passes the cylinder–flare junction; and the growth of reseparation along the line of the cylinder–flare junction once the spot base flow falls to a sufficiently low turbulent or laminar state. The results suggest that both mechanisms have comparable time scales.

At the stage where the inboard flow is attached, the progressive separation collapse results in a large pressure difference with respect to the outboard separation. The wave interaction model in this paper describes how the resultant transient wave system must develop, and provides a mechanism for the progressive loss of the separation and reattachment shock waves, as well as the initiation and growth of the attached junction shock. This integrates well with the heat transfer, pressure and schlieren data.

The primary focus of this paper concerned the isolated spot interaction. However, limited test data at higher spot passage rates suggest that for important characteristics, such as peak heating and maximum width, there is a relatively smooth transition from the isolated spot, through trains of amalgamating disturbances, to the fully turbulent wedge. The collapse–reseparation process remains the same, but at any instant it can be truncated by interaction with preceding/following spots.

Funding. This work was supported by the Engineering and Physical Sciences Research Council (EPSRC) UK, grant EP/H020853/1.

Declaration of interests. The authors report no conflict of interest.

Author ORCIDs.
David Estruch-Samper https://orcid.org/0000-0001-6392-9691;
Leon Vanstone https://orcid.org/0000-0001-7797-7133.

References

Babinsky, H. & Harvey, J.K. 2014 *Shock Wave–Boundary-Layer Interactions*. Cambridge Aerospace Series. Cambridge University Press.

Ben-Artzi, M. & Falcovitz, J. 1984 A second-order Godunov-type scheme for compressible fluid dynamics. *J. Comput. Phys.* **55**, 1–32.

Berry, S.A. & Horvath, T.J. 2008 Discrete-roughness transition for hypersonic flight vehicles. *J. Spacecr. Rockets* **45**, 216–227.

Butler, C. & Laurence, S.J. 2020 Interaction of hypersonic boundary-layer instability waves with axisymmetric compression and expansion corners. In *Proc. AIAA Aviation 2020 Forum, Virtual Event*, 15–19 June 2020. *AIAA Paper* 2020-3071.

Casper, K.M., Beresh, S.J., Henfling, J.F., Spillers, R.W., Hunter, P. & Spitzer, S. 2018 Hypersonic fluid-structure interactions due to intermittent turbulent spots on a slender cone. *AIAA J.* **57** (2), 749–759.

Casper, K.M., Beresh, S.J. & Schneider, S.P. 2014 Pressure fluctuations beneath instability wave packets and turbulent spots in a hypersonic boundary layer. *J. Fluid Mech.* **756**, 1058–1091.

Chuvakhov, P.V., Fedorov, A.V. & Obraz, A.O. 2018 Numerical simulation of turbulent spots generated by unstable wave packets in a hypersonic boundary layer. *Comput. Fluids* **162**, 26–38.

Cook, W.J. & Felderman, E.J. 1966 Reduction of data from thin-film heat-transfer gauges: a concise numerical technique. *AIAA J.* **4**, 561–562.

Denman, P.A. 1996 Experimental study of hypersonic boundary layers and base flows. PhD thesis, University of London.

Dwivedi, A., Sidharth, G.S., Nichols, J.W., Candler, G.V. & Jovanovic, M.R. 2019 Reattachment streaks in hypersonic compression ramp flow: an input–output analysis. *J. Fluid Mech.* **880**, 113–135.

EMMONS, H.W. 1951 The laminar-turbulent transition in a boundary layer. Part I. *J. Aeronaut. Sci.* **18** (7), 490–498.

ESTRUCH-SAMPER, D., HILLIER, R., VANSTONE, L. & GANAPATHISUBRAMANI, B. 2017 Effect of isolated roughness element height on high-speed laminar–turbulent transition. *J. Fluid Mech.* **818**, R1.

EUROPEAN SPACE AGENCY (ESA) 2011 Skylon assessment report. *Propulsion & Aerothermodynamics Division, Directorate of Technology, Engineering and Quality, ESA*. TEC-MPC/2011/946/MF, pp. 1–52.

FEDOROV, A. 2011 Transition and stability of high-speed boundary-layers. *Annu. Rev. Fluid Mech.* **818**, 79–95.

FEDOROV, A. & TUMIN, A. 2017 Receptivity of high-speed boundary layers to kinetic fluctuations. *AIAA J.* **55** (7), 2335–2348.

FIALA, A., HILLIER, R. & ESTRUCH-SAMPER, D. 2014 Roughness-induced turbulent wedges in a hypersonic blunt-body boundary layer. *J. Fluid Mech.* **754**, 208–231.

FIALA, A., HILLIER, R., MALLINSON, S.G. & WIJENSINGHE, H.S. 2006 Heat transfer measurement of turbulent spots in a hypersonic blunt-body boundary layer. *J. Fluid Mech.* **555**, 81–111.

FISCHER, M.C. 1972 Spreading of a turbulent disturbance. *AIAA J.* **10**, 957–959.

FRANKO, K.J. & LELE, S.K. 2013 Breakdown mechanisms and heat transfer overshoot in hypersonic zero pressure gradient boundary layers. *J. Fluid Mech.* **730**, 491–532.

GAD-EL-HAK, M., BLACKWELDER, R.F. & RILEY, J.J. 1981 On the growth of turbulent regions in laminar boundary layers. *J. Fluid Mech.* **110**, 73–95.

HADER, C. & FASEL, H.F. 2019 Direct numerical simulations of hypersonic boundary-layer transition for a flared cone: fundamental breakdown. *J. Fluid Mech.* **869**, 341–384.

HEIN, S., THEISS, A., DI GIOVANNI, A., STEMMER, C., SCHILDEN, T., SCHRODER, W., PAREDES, P., CHOUDHARI, M.M., LI, F. & RESHOTKO, E. 2019 Numerical investigation of roughness effects on transition on spherical capsules. *J. Spacecr. Rockets* **56** (2), 388–404.

HILLIER, R. 2007 Shock-wave/expansion-wave interactions and the transition between regular and Mach reflection. *J. Fluid Mech.* **575**, 399–424.

HORVATH, T.J., ZALAMEDA, J.N., WOOD, W.A., BERRY, S.A., SCHWARTZ, R.J., DANTOWITZ, R.F., SPISZ, T.S. & TAYLOR, J.C. 2012 Global infrared observations of roughness induced transition on the Space Shuttle orbiter. NATO RTO-MP-AVT-200, pp. 1–22.

JACKSON, A.P., HILLIER, R. & SOLTANI, S. 2001 Experimental and computational study of laminar cavity flows at hypersonic speeds. *J. Fluid Mech.* **427**, 329–358.

JEWELL, J.S., LEYVA, I.A. & SHEPHERD, J.E. 2017 Turbulent spots in hypervelocity flow. *Exp. Fluids* **58**, 32.

JULIANO, T.J., JEWELL, J.S., KIMMEL, R.L. 2021 HIFiRE-5b boundary-layer transition length and turbulent overshoot. *J. Spacecr. Rockets* **58** (2), 265–283.

KEYES, F.G. 1952 The heat conductivity, viscosity, specific heat and Prandtl numbers for thirteen gases. *Tech. Rep.* 37. Massachussetts Institute of Technology, Project Squid.

KIMMEL, R.L., ADAMCZAK, D.W., HARTLEY, D., ALESI, H., FROST, M.A., PIETSCH, R., SHANNON, J. & SILVESTER, T. 2018 Hypersonic international flight research experimentation-5b flight overview. *J. Spacecr. Rockets* **55** (6), 1303–1314.

KRISHNAN, L. & SANDHAM, N.D. 2006 Effect of Mach number on the structure of turbulent spots. *J. Fluid Mech.* **566**, 225–234.

KRISHNAN, L. & SANDHAM, N.D. 2007 Strong interaction of a turbulent spot with a shock-induced separation bubble. *Phys. Fluids* **19**, 016102.

LADERMAN, A.J. 1980 Adverse pressure gradient effects on supersonic boundary-layer turbulence. *AIAA J.* **18**, 1186–1195.

LEE, C. & JIANG, X. 2019 Flow structures in transitional and turbulent boundary layers. *Phys. Fluids* **31**, 111301.

LEIDY, A.N., RESHOTKO, E., SIDDIQUI, F. & BOWERSOX, R.D.W. 2017 Transition due to roughness on blunt capsule: comparison with transient growth correlation. *J. Spacecr. Rockets* **55** (1), 167–180.

MACK, L.M. 1984 Boundary layer linear stability theory. In *Special Course on Stability and Transition of Laminar Flow*. *AGARD Rep.* 709, vol. 3, pp. 1–81.

MALLINSON, S.G., HILLIER, R., JACKSON, A.P., KIRK, D.C., SOLTANI, S. & ZANCHETTA, M. 2000 Gun tunnel flow calibration: defining input conditions for hypersonic flow computations. *Shock Waves* **10**, 313–322.

MEE, D.J. 2002 Boundary-layer transition measurements in hypervelocity flows in a shock tunnel. *AIAA J.* **40**, 1542–1548.

MURRAY, N., HILLIER, R. & WILLIAMS, S. 2013 Experimental investigation of axisymmetric hypersonic shock-wave/turbulent-boundary-layer interactions. *J. Fluid Mech.* **714**, 152–189.

NARASIMHA, R. 1985 The laminar-turbulent transition zone in the turbulent boundary layer. *Prog. Aerosp. Sci.* **22**, 29–80.

NOVIKOV, A., EGOROV, I. & FEDOROV, A. 2016 Direct numerical simulation of wave packets in hypersonic compression-corner flow. *AIAA J.* **54** (7), 2034–2050.

PAREDES, P., CHOUDHARI, M. & LI, F. 2020*a* Mechanism for frustum transition over blunt cones at hypersonic speeds. *J. Fluid Mech.* **894**, A22.

PAREDES, P., CHOUDHARI, M., LI, F., JEWELL, J.S., KIMMEL, R.L., MARINEAU, E.C. & GROSSIR, G. 2020*b* Nosetip bluntness effects on transition at hypersonic speeds: experimental and numerical analysis. Chapter 7 in Hypersonic Boundary-Layer Transition Prediction. *NATO Tech. Rep.* NTO-STO-TR-AVT-240, pp. 1–36.

PERRY, A.E., LIM, T.T. & TEH, E.W. 1981 A visual study of turbulent spots. *J. Fluid Mech.* **104**, 387–405.

RADESPIEL, R., ALI, S.R.C., MUNOZ, F., BOWERSOX, R., LEIDY, A., TANNO, H., KIRK, L.C. & RESHOTKO, E. 2018 Experimental investigation of roughness effects on transition on blunt spherical capsule shapes. *J. Spacecr. Rockets* **56** (2), 405–420.

REDFORD, J.A., SANDHAM, N.D. & ROBERTS, G.T. 2012 Numerical simulations of turbulent spots in supersonic boundary layers: effects of Mach number and wall temperature. *Prog. Aerosp. Sci.* **52**, 67–79.

RESHOTKO, E. 2001 Transient growth: a factor in bypass transition. *Phys. Fluids* **13** (5), 1067–1075.

ROBBINS, B.A., CASPER, K.M. & MESH, M. 2019 Quantifying the structural response of a slender cone to turbulent spots at Mach 6. In *Proc. AIAA Scitech 2019 Forum*, 7–11 January 2019, San Diego, California, USA. *AIAA Paper* 2019-1631.

ROSHKO, A. & THOMKE, G.J. 1966 Observations of turbulent reattachment behind an axisymmetric downstream-facing step in supersonic flow. *AIAA J.* **4** (6), 975–980.

SCHNEIDER, S.P. 2008 Effects of roughness on hypersonic boundary-layer transition. *J. Spacecr. Rockets* **45** (2), 193–209.

SCHULTZ, D.L. & JONES, T.V. 1973 Heat-transfer measurements in short-duration hypersonic facilities. *AGARDograph* 165.

SEIFERT, A. & WYGNANSKY, L. 1995 On turbulent spots in a laminar boundary layer subjected to a self-similar adverse pressure gradient. *J. Fluid Mech.* **296**, 185–209.

SIVASUBRAMANIAN, J. & FASEL, H.F. 2015 Direct numerical simulation of transition in a sharp cone boundary layer at Mach 6: fundamental breakdown. *J. Fluid Mech.* **768**, 175–218.

TUMIN, A. 2007 Outlook for theoretical modelling of isolated roughness-induced perturbations in turbulent boundary layers. In *Proceedings of the 37th AIAA Fluid Dynamics Conference and Exhibit*, 25–28 June 2007, Miami, FL, USA. *AIAA Paper* 2007-3993.

TUMIN, A. 2008 Nonparallel flow effects on roughness-induced perturbations in boundary layers. *J. Spacecr. Rockets* **45** (6), 1176–1184.

WHALEN, T.J., SCHONEICH, A.G., LAURENCE, S.J., SULLIVAN, B.T., BODONY, D.J., FREYDIN, M., DOWELL, E.H. & BUCK, G.M. 2020 Hypersonic fluid-structure interactions in compression corner shock-wave/boundary-layer interaction. *AIAA J.* **58** (9), 4090–4105.

WHEATON, B.M., BARTKOWICZ, M.D., SUBBAREDDY, P.K., SCHNEIDER, S.P. & CANDLER, G.V. 2011 Roughness-induced instabilities at Mach 6: a combined numerical and experimental study. In *Proceedings of the 41st AIAA Fluid Dynamics Conference and Exhibit*, 27–30 June 2011, Honolulu, Hawaii, USA. *AIAA Paper* 2011-3248.

WHEATON, B.M., BERRIDGE, D.C., WOLF, T., ARAYA, D., STEVENS, R., MCGRATH, B.E., KEMP, B. & ADAMCZAK, D. 2021 Final design of the Boundary Layer Transition (BOLT) flight experiment. *J. Spacecr. Rockets* **58** (1), 6–17.